26694

National Library of Canada | Bibliothèque nationale du Canada

CANADIAN THESES ON MICROFICHE | THÈSES CANADIENNES SUR MICROFICHE

NAME OF AUTHOR/NOM DE L'AUTEUR JOHN DOUGLAS ALEXANDER

TITLE OF THESIS/TITRE DE LA THÈSE SATELLITE DATA ANALYSIS OF ARCTIC 500-MB LOWS.

UNIVERSITY/UNIVERSITÉ UNIVERSITY OF ALBERTA

DEGREE FOR WHICH THESIS WAS PRESENTED/GRADE POUR LEQUEL CETTE THÈSE FUT PRÉSENTÉE MASTER OF SCIENCE

YEAR THIS DEGREE CONFERRED/ANNÉE D'OBTENTION DE CE GRADE 1975

NAME OF SUPERVISOR/NOM DU DIRECTEUR DE THÈSE DR. E.R. REINELT

Permission is hereby granted to the NATIONAL LIBRARY OF CANADA to microfilm this thesis and to lend or sell copies of the film.

The author reserves other publication rights, and neither the thesis nor extensive extracts from it may be printed or otherwise reproduced without the author's written permission.

L'autorisation est, par la présente, accordée à la BIBLIOTHÈQUE NATIONALE DU CANADA de microfilmer cette thèse et de prêter ou de vendre des exemplaires du film.

L'auteur se réserve les autres droits de publication; ni la thèse ni de longs extraits de celle-ci ne doivent être imprimés ou autrement reproduits sans l'autorisation écrite de l'auteur.

DATED/DATÉ October 6, 1975 SIGNED/SIGNÉ John D. Alexander

PERMANENT ADDRESS/RÉSIDENCE FIXE 915 CONIFER ST.
SHERWOOD PARK ALBERTA

NL-91 (3-74)

THE UNIVERSITY OF ALBERTA

SATELLITE DATA ANALYSIS OF ARCTIC 500-MB. LOWS

by

JOHN DOUGLAS ALEXANDER (C)

A THESIS

SUBMITTED TO THE FACULTY OF GRADUATE STUDIES AND RESEARCH

IN PARTIAL FULFILMENT OF THE REQUIREMENTS FOR THE DEGREE

OF MASTER OF SCIENCE

IN

METEOROLOGY

DEPARTMENT OF GEOGRAPHY

EDMONTON, ALBERTA

FALL, 1975

THE UNIVERSITY OF ALBERTA

FACULTY OF GRADUATE STUDIES AND RESEARCH

The undersigned certify that they have read, and recommend to the Faculty of Graduate Studies and Research, for acceptance, a thesis intitled "Satellite Data Analysis of Arctic 500-mb. Lows", submitted by John Douglas Alexander in partial fulfilment of the requirements for the degree of Master of Science in Meteorology.

E. K. Reinelt
.....
Supervisor

Robert Elliott
.....

.....

.....

Date 2 October 1975

DEDICATED TO

My wife, Diane, for her patience and encouragement,

to my daughter, Shawna

and to our anticipated new arrival.

ABSTRACT

Intense and persistent cyclonic vortices frequently dominate the atmospheric circulation to high levels over Arctic areas. With the aid of satellite infrared images, this study examines some aspects of these systems.

From analyses prepared by the Canadian Meteorological Centre (C.M.C.) 500-mb. cyclone tracks are plotted for a twelve-month period from June, 1973 to May, 1974. The NOAA ITOS Satellite images used in this study were received by the Satellite Laboratory at the University of Alberta. A brief discussion of some characteristics of these images is presented, as well as some basic information on the recognition of cloud types and clear areas.

Selected cases were chosen from the summer months of July, August and September, 1973. Moisture and temperature distributions are derived using a simple cloud-band model for the cloud masses surrounding these deep vortices.

Two methods of vertical velocity computation are examined in this study, namely the vorticity and the omega equation techniques. A 12 x 12 grid, with a grid-

length of 381 km., is established over the Canadian Arctic. A test-field of geopotential gridpoint height data is used in the vertical velocity computations for comparison of the two techniques. C.M.C. gridpoint height data are then used to compute vertical velocities and compare the two methods for a two-week period in July, 1973. Combinations of vertical velocity and moisture ranges are presented in tabular form for clear and cloudy areas determined from the appropriate satellite images. For the vorticity method, correlations of cloud with moisture and ascent, or of clear areas with descent and no moisture appear poor. From the omega equation results, the ascent - cloud and descent - clear correlations are improved. Both clear categories for moisture thickness (M) 0 to 2000 feet show more subsidence than ascent. For middle cloud with $M \geq 8000$ feet, more cases of ascent are observed. However, for low cloud with $2000 \leq M < 8000$ feet, more subsidence occurrs.

Finally, a case study is examined to relate synoptic features and cloud masses from satellite images.

ACKNOWLEDGEMENTS

I wish to thank Dr. E. R. Reinelt for his helpful guidance throughout this study. Thanks are also due to Dr. R. Charlton and Dr. K. Smillie who, with Dr. Reinelt, were on my examining committee.

I wish to thank my wife Diane for typing the final draft, and the Departmental Photographers and the staff of the Meteorological Satellite Laboratory of the University of Alberta for their assistance. I also thank Mr. W. Hume for his assistance in the adaptation of the omega equation program to this study.

This study was undertaken while on Education Leave from the Atmospheric Environment Service, Environment Canada.

TABLE OF CONTENTS

		Page
DEDICATION		iv
ABSTRACT		v
ACKNOWLEDGEMENTS		vii
TABLE OF CONTENTS		viii
LIST OF TABLES		xi
LIST OF FIGURES		xii
CHAPTER		
I	SYNOPTIC AND THEORETICAL CONSIDERATIONS	1
1.1	Introduction	1
1.2	General Specifications of Satellite Photos Used	2
1.3	The Use of Satellite Photos in Cloud Analysis	5
1.4	Vertical Velocity Calculation	8
1.4.1	Description of the Finite Difference Grid	8
1.4.2	Vertical Velocity: The Vorticity Method	10
1.4.3	Vertical Velocity: The Omega Equation	14
1.4.4	Vertical Structure for Omega Equation	18
1.4.5	Omega Equation Solution	20
1.5	Statistical Treatment of the Results	22

CHAPTER

II SOURCES AND METHODS OF OBSERVATIONS ... 28

2.1 500-mb Cyclone Tracks 28

2.2 Selected Cases of 500-mb. Cyclone Tracks for Moisture and Temperature Analysis .. 30

2.3 Vertical Velocity Calculations 46

III MOISTURE, TEMPERATURE AND VERTICAL VELOCITY RESULTS 48

3.1 Moisture and Temperature Distributions Associated with 500-mb. Lows 48

3.1.1 Dewpoint Depressions 48

3.1.2 Surface Dewpoint Depressions ... 48

3.1.3 850-mb. Dewpoint Depressions ... 49

3.1.4 700-mb. Dewpoint Depressions ... 55

3.1.5 500-mb. Dewpoint Depressions ... 55

3.1.6 Minimum Dewpoint Depressions ... 56

3.1.7 Moist Layer Thicknesses 56

3.1.8 Vertical Temperature Differences 60

3.1.9 The "Log-Normal" Transformation 65

3.2 The Vertical Velocity Calculations 65

3.2.1 Vertical Velocity Programs' Test 65

3.2.2 Vertical Velocity, Moisture and Cloud 73

IV CASE STUDY 23/1200Z, JULY, 1973 81

4.1 Introduction 81

4.2 Surface Analysis 81

4.3 850-mb. Analysis 85

4.4 700-mb. Analysis 85

	4.5	500-mb. Analysis	88
	4.6	Vertical Velocity - Low Level	88
	4.7	Vertical Velocity - Middle Level	92
V		PROBLEMS ENCOUNTERED AND SUGGESTIONS FOR IMPROVEMENTS	93
	5.1	Cloud Classification	93
	5.2	Vertical Velocity - Cloud Correlations	94
VI		SUMMARY AND CONCLUSIONS	99
BIBLIOGRAPHY			105
APPENDIX: A "LOG-NORMAL" TRANSFORMATION			107

LIST OF TABLES

Table	Description	Page
I	500-mb. low cases chosen for moisture and temperature analysis using satellite photographs	31
II	Dewpoint depression statistics for low, middle cloud and clear areas	50
III	Minimum dewpoint depression and moist layer statistics for low, middle cloud and clear areas	58
IV	Vertical temperature difference statistics for low, middle cloud and clear areas	64
V	Percentage occurrences of combinations of vertical velocity (by vorticity method) and moist layer thickness ranges	74
VI	Percentage occurrences of moist layer thickness ranges	75
VII	Percentage occurrences of vertical velocity ranges using vorticity method	76
VIII	Same as Table V, except using the omega equation vertical velocity results	77
IX	Same as Table VII, except using omega equation vertical velocity results	78

LIST OF FIGURES

Figure		Page
1	Scan of Earth's surface by infrared scanner (Anderson et al 1973)	4
2	NOAA-2, 3307, 06/1945Z, July, 1973	7
3	Map of 12 x 12 grid	9
4	Gridpoint (i,j) and four neighbouring gridpoints	13
5	Gridpoint (i,j,) and eight neighbouring gridpoints	17
6	Vertical structure for omega equation solution	19
7	Schematic diagrams to illustrate skewness and kurtosis	25
8	500-mb. cyclone tracks for June, July 1973	32
9	500-mb. cyclone tracks for August, September 1973	33
10	500-mb. cyclone tracks for October, November 1973	34
11	500-mb. cyclone tracks for December, 1973, January 1974	35
12	500-mb. cyclone tracks for February, March 1974	36
13	500-mb. cyclone tracks for April, May 1974	37
14	Cloud band model (Adapted from Shenk and Brooks, 1965)	39
15	NOAA-2, 3543, 25/1620Z, July, 1973	41
16	Adjustment of cloud pattern for satellite photo-upper air observation time difference	44

Figure		Page
17	Surface dewpoint depression distributions	51
18	850-mb. dewpoint depression distributions	52
19	700-mb. dewpoint depression distributions	53
20	500-mb. dewpoint depression distributions	54
21	Minimum dewpoint depression distributions	57
22	Moist-layer thickness distributions	59
23	Temperature (surface) - temperature (850 mb.) distributions	61
24	Temperature (850 mb.) - temperature (700 mb.) distributions	62
25	Temperature (700 mb.) - temperature (500 mb.) distributions	63
26	Dewpoint depression frequencies and transformed variable frequencies	66
27	Model atmosphere for testing vorticity and omega equation methods of vertical velocity calculations	68
28	850-mb. and 700-mb. vertical velocities generated by the vorticity method for the test field	69
29	Same as Fig. 28 except for 500 mb. and 300 mb.	70
30	775-mb. and 600-mb. vertical velocities generated by the omega equation for the test field	71
31	Same as Fig. 30 except for 400 mb.	72
32	Locations of Radiosonde stations and surface analysis for 23/1200Z, July, 1973	82
33	NOAA-2, 3518, 23/1620Z, July, 1973	83
34	NOAA-2, 3521, 23/2200Z, Jyly, 1973	84
35	850-mb. contour charts for 23/1200Z, July, 1973	86

Figure		Page
36	700-mb. contour charts for 23/1200Z, July, 1973	87
37	500-mb. contour and vorticity chart for 23/1200Z, Jyly, 1973	89
38	Vertical velocity field by vorticity method at 850 and 700 mb. and low and middle cloud for 23/1200Z, July, 1973	90
39	Vertical velocity field by omega equation method at 775 and 600 mb. and low and middle cloud for 23/1200Z, July, 1973	91

CHAPTER I

SYNOPTIC AND THEORETICAL CONSIDERATIONS

1.1 Introduction

Since 500-mb. cyclonic systems occur in all seasons and often dominate the circulation over the entire Canadian Arctic, any new information on the structure of these systems is valuable. The analysis and forecasting of meteorological parameters associated with such systems is often complicated and in some cases all but impossible because of a lack of surface and upper air data. Fortunately, with the launching of meteorological satellites in recent years, the situation has somewhat improved, and satellite photos are now available to augment the sparse data from the few conventional observation sites in the Arctic.

This investigation consists of four main sections. The first section presents monthly charts of 500-mb. cyclone tracks for the period from June, 1973 to May, 1974. These charts are chosen to illustrate the persistence and frequently erratic motion of these systems. The second section deals with the moisture and temperature distributions in various areas near the upper disturbance, according to a cloud-band

model described in Chapter II. The third section is concerned with the patterns of vertical velocity and moisture as manifested in satellite images over the Arctic. The final section presents a case study in which the satellite cloud observations are compared to several analyses of meteorological fields at various levels.

1.2 General Specifications of Satellite Photos Used

The satellite photographs used in this study were received and processed at the Meteorological Satellite Laboratory of the University of Alberta. The pictures obtained were from the U.S. National Oceanic and Atmospheric Administration satellite NOAA-2, orbiting at 790 nautical miles above the Earth. Since only infrared images were used in this study, the following discussion will centre on the characteristics and specifications of the infrared images. The material for this and the subsequent section of cloud analysis has been taken from Anderson et al (1973).

The satellite scanning radiometer measures radiation in the 10.5 to 12.5 μm. spectrum range with the measurements converted to different shades of grey. Since the long-wave radiation emitted by the Earth's surface and clouds varies according to the temperature

of the radiating surface, the darkest areas on the infrared photos correspond to the warmest radiating surfaces while the whitest areas correspond to the coldest surfaces.

The scanning radiometer scans perpendicularly to the satellite path, from horizon to horizon. This causes considerable distortion of the picture along the edges and reduces the reliable data portion of the picture to approximately 80 percent of the distance from the centre of the picture to its edge. In Figure 1 below, the geometry of the scan is shown with the Earth's curved surface displayed on the flat image plane of the infrared scanner. The image plane is divided into eight equal segments, with the number above each segment indicating the length in nautical miles of the arc of the Earth's surface included in that segment. The numbers shown below the curved Earth's Surface indicate the instrument resolution. It ranges from 4.0 nautical miles to 14.7 nautical miles, beyond which the resolution decreases markedly while the distortion increases rapidly. This restricts the reliable data region to the inner 860 nautical miles of the scan, which is approximately 80 percent of the distance from the image centre to the image edge, as stated previously.

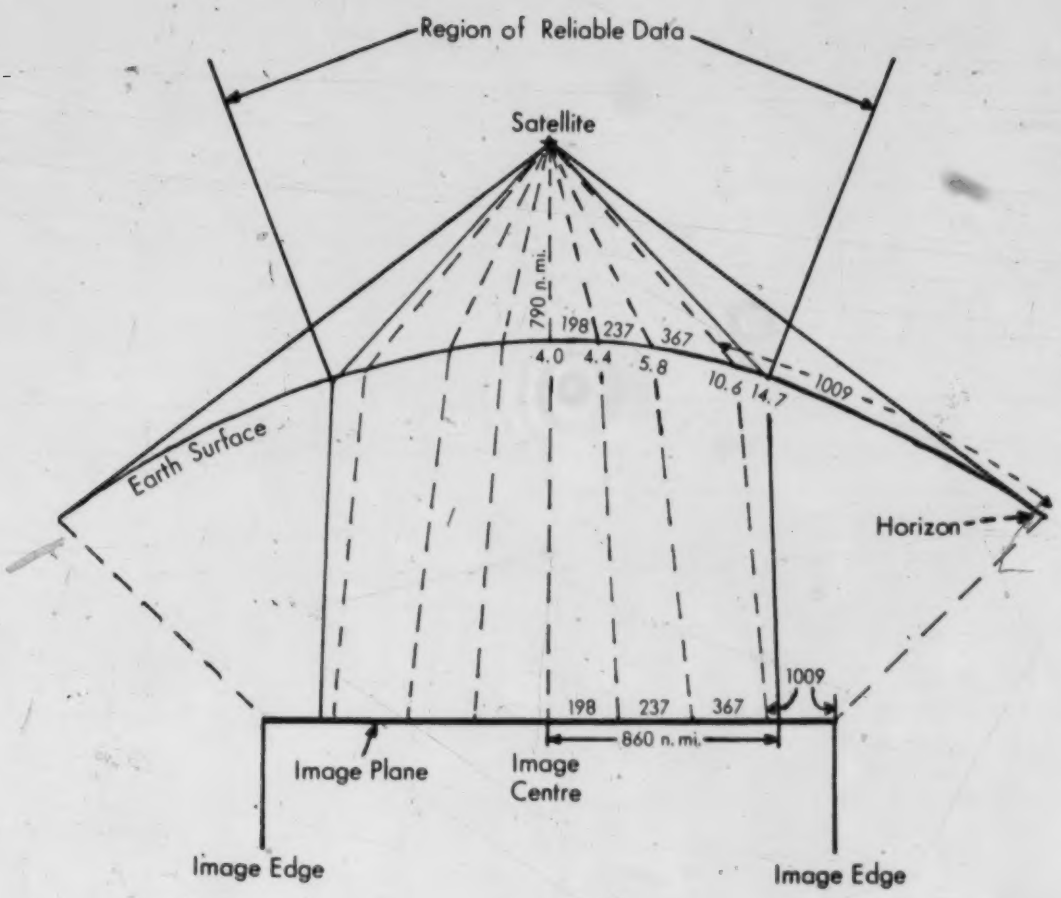

Fig. 1. Scan of the Earth's curved surface displayed on the flat image plane of the infrared scanner. (Anderson, R.K. et al 1973, p.4).

1.3 The Use of Satellite Photos in Cloud Analysis

The following remarks concern the appearance of low and middle cloud, and clear areas as recorded on infrared satellite images. The basis for the discrimination between low and middle cloud is the different shades of grey which cloudy areas show relative to cloud-free land or water areas.

Low cloud areas such as stratocumulus or stratus, not obscured by higher clouds, generally appear grey, because the tops of the low clouds are cooler than the land areas, which appear as darker shades of grey. However, problems can occur with this method of discriminating low cloud areas when the tops of the radiating clouds are at a temperature nearly equal to the adjacent land or water areas, because the clear and cloudy areas exhibit then similar shades of grey. This difficulty is alleviated to some extent in the Canadian Arctic by the large number of islands and areas of open water in the summer, which provide good contrast to the coastlines. Thus, an overlying area of low cloud which may be radiating at the land or water temperature will still obscure the coastlines, and so be readily differentiated.

However, with winter and spring satellite images, the cloud determination is much more difficult.

Absence of a strong Earth-cloud temperature difference would make the cloud type difficult to ascertain from the grey shade variations alone. Also, with only a few open leads present, the temperature discontinuity along coastlines cannot readily be used as a clue to the presence of cloud.

Middle cloud areas such as altostratus, altocumulus and nimbostratus appear light grey to white, because of their generally high, cold radiating tops. The main problem in identifying middle cloud is possible confusion with cirrus or cirrostratus, since cirriform cloud types can also appear as light grey or white images. Erroneous classification could result if no middle cloud layer existed under the high cloud. However, this may not be a serious problem, since frequently well-organized bands of thick, high cloud have layers of cloud below them also. Finally, the determination of clear areas on satellite images is a relatively straightforward process, since the land areas in summer are generally warm, and consequently appear very dark in the photos. The coastlines, as previously mentioned, also show a good contrast, a fact that further assists in determining the cloudless areas. Figure 2 shows a sample image illustrating low and middle cloud, and clear areas.

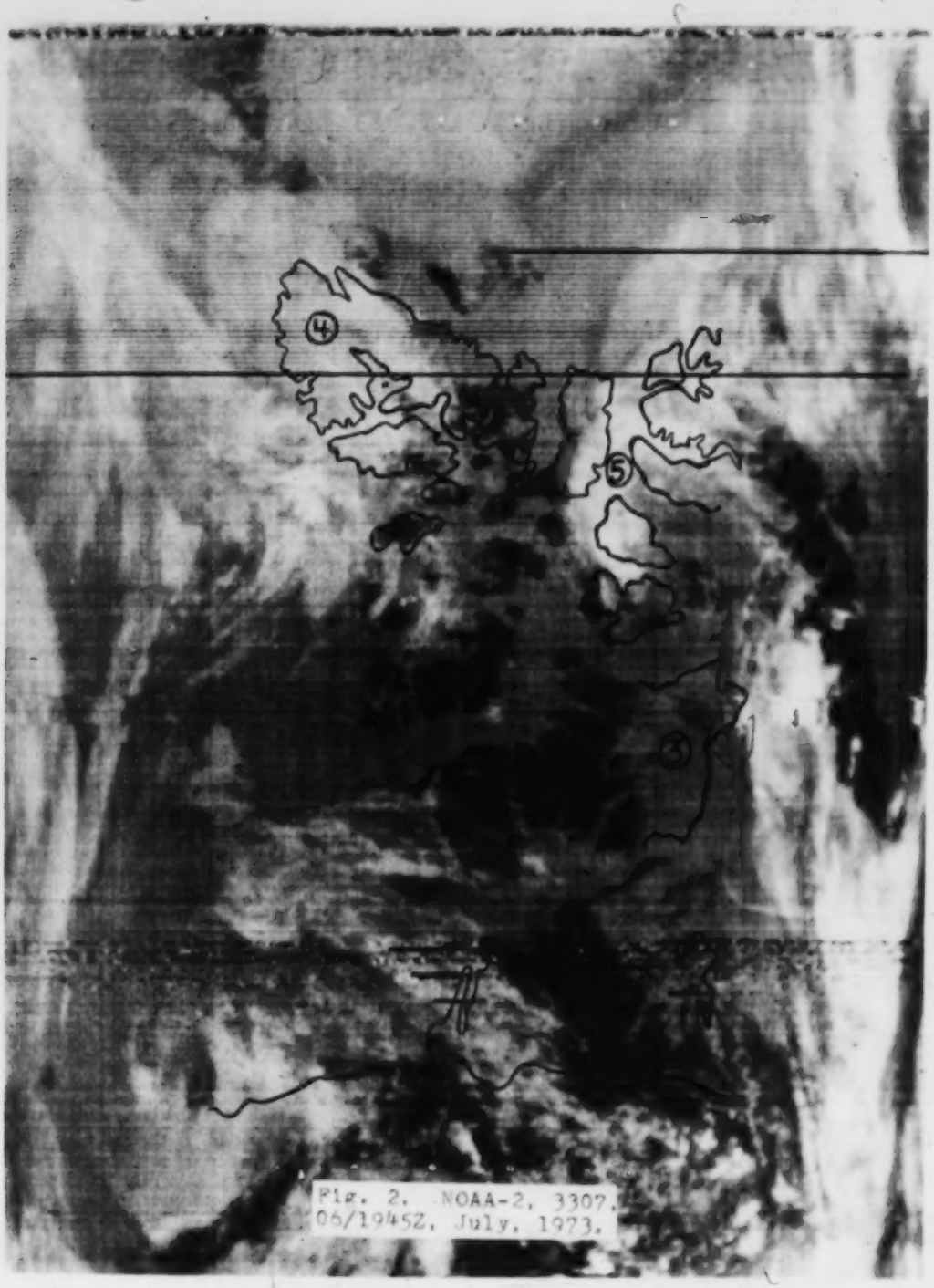

Fig. 2. NOAA-2, 3307.
06/1945Z, July, 1973.

Geographical outlines have been drawn only where cloud obscures coastlines. In the cloudless areas, several islands are clearly visible, as for example, the northern parts of Victoria Island (1) and Banks Island (2). Low-cloud covers southern Victoria Island (3) and northern Ellesmere Island (4). Here the shading of the cloudy areas is a light grey, similar to that of the open water, or areas between islands covered by ice. However, the absence in such areas of the contrasting coastlines means that they are obscured by cloud. A middle cloud area is that labelled (5), where the higher, colder tops radiating at a lower temperature are producing a shade of almost pure white.

1.4 Vertical Velocity Calculation

1.4.1 Description of Finite-Difference Grid

The 12 x 12 grid used in the finite-difference calculations is shown in Figure 3 below. The grid interval is 381 km. at the 60°N latitude standard. The inner dashed line indicates the 8 x 8 gridpoints at which vertical velocities were calculated. The upper left hand corner of the grid is labelled (1,1) with the i and j indices increasing along the directions of the arrows shown.

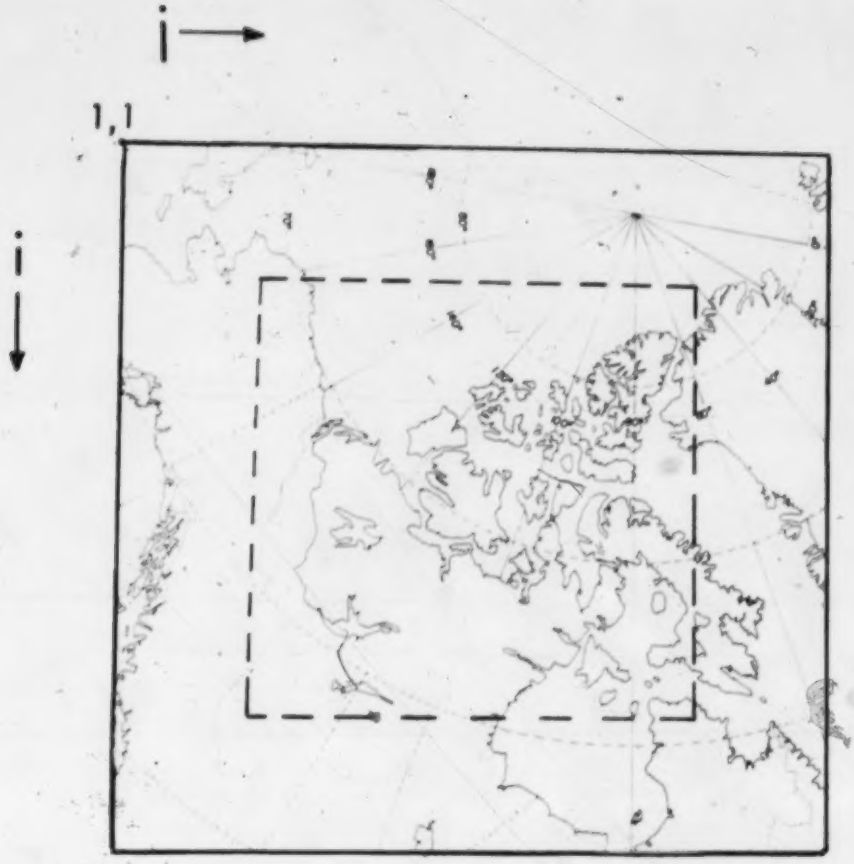

Fig. 3. Map of 12 x 12 grid (outer solid line) and 8 x 8 grid (inner dashed line). Origin of grid is labelled "1,1".

1.4.2 Vertical Velocity: The Vorticity Method:

One of the methods used to compute vertical velocities is the vorticity method. The derivation given below is based on that given by Petterssen (1956).

The vorticity equation referred to isobaric surfaces using pressure as the vertical coordinate is:

$$\frac{\partial Q_p}{\partial t}+u\frac{\partial Q_p}{\partial x}+v\frac{\partial Q_p}{\partial y}+\omega\frac{\partial Q_p}{\partial p}=-D_p Q_p+q_x\frac{\partial \omega}{\partial x}+q_y\frac{\partial \omega}{\partial y} \qquad 1.1$$

where Q_p is the absolute vorticity with respect to a constant pressure surface,

D_p is the divergence with respect to a constant pressure surface,

$\omega \equiv dp/dt$ is the generalized vertical velocity using pressure as the vertical coordinate,

q_x and q_y are the horizontal components of the relative vorticity,

and u and v are the horizontal wind components.

The equation of continuity in an (x,y,p,t) system is

$$D_p=-\frac{\partial \omega}{\partial p} \qquad 1.2$$

Substituting (1.2) into equation (1.1), and dropping the subscript p results in

$$\frac{\partial Q}{\partial t}+u\frac{\partial Q}{\partial x}+v\frac{\partial Q}{\partial y}+\omega\frac{\partial Q}{\partial p}=\frac{\partial \omega}{\partial p}Q+q_x\frac{\partial \omega}{\partial x}+q_y\frac{\partial \omega}{\partial y} \qquad 1.3$$

From the relation

$$Q^2\frac{\partial}{\partial p}\left(\frac{\omega}{Q}\right)=Q^2\left(\frac{1}{Q}\right)\frac{\partial \omega}{\partial p}-Q^2\frac{\omega}{Q^2}\frac{\partial Q}{\partial p}$$

$$= Q\frac{\partial w}{\partial p} - w\frac{\partial Q}{\partial p} \qquad 1.4$$

it follows that

$$\frac{\partial Q}{\partial t} + u\frac{\partial Q}{\partial x} + v\frac{\partial Q}{\partial y} = Q^2\frac{\partial}{\partial p}\left(\frac{w}{Q}\right) + q_x\frac{\partial w}{\partial x} + q_y\frac{\partial w}{\partial y} \qquad 1.5$$

Also, in the free atmosphere, the terms $q_x\frac{\partial w}{\partial x} + q_y\frac{\partial w}{\partial y}$ are usually small and so may be neglected:

$$\frac{w_1}{Q_1} - \frac{w_0}{Q_0} = \int_0^1 \frac{\partial Q/\partial t + u\,\partial Q/\partial x + v\,\partial Q/\partial y}{Q^2}\,\delta p \qquad 1.6$$

where subscript 1 refers to an upper level,

subscript 0 refers to a lower level.

The mean value theorem may be used to evaluate the integral as follows:

$$\frac{w_1}{Q_1} = \frac{w_0}{Q_0} + \left[\overline{\frac{\partial Q/\partial t + u\,\partial Q/\partial x + v\,\partial Q/\partial y}{Q^2}}\right]\ (p_1 - p_0) \qquad 1.7$$

where the bar refers to the mean of the function within the square brackets between the levels p_1 and p_0.

The lowest level is taken to be 1000 mb. and the vertical velocity at 1000 mb. is assumed to be zero. The values of w were computed at 850 mb., 700 mb., 500 mb. and 300 mb.

In order to evaluate equation (1.7), the vorticity must be known; the true vorticity can be approximated

by calculating the geostrophic vorticity

$$Q_g = \frac{g}{\#} \nabla^2 Z + f \qquad 1.8$$

where $\nabla^2 Z$ is the Laplacian of the geopotential height field Z,

f is the Coriolis parameter,

and g is the gravitational acceleration.

The wind components u and v are calculated from the geostrophic wind equations:

$$u_g = -g/f \frac{\partial Z}{\partial y} \qquad v_g = g/f \frac{\partial Z}{\partial x} \qquad 1.9$$

The computations are performed using finite-difference formulae as shown below for a gridpoint (i,j) as in Figure 4. The finite difference formulae evaluated at gridpoint (i,j) are:

$$(u_g)_{i,j} = -\frac{g m(i,j)}{f(i,j)} \left(\frac{Z(i+1,j) - Z(i-1,j)}{2H} \right) \qquad 1.10$$

$$(v_g)_{i,j} = \frac{g m(i,j)}{f(i,j)} \left(\frac{Z(i,j+1) - Z(i,j-1)}{2H} \right) \qquad 1.11$$

$$(Q_g)_{i,j} = \frac{g m(i,j)^2}{f(i,j)} \left(\frac{Z(i,j-1) + Z(i+1,j) + Z(i,j+1) + Z(i-1,j) - 4Z(i,j)}{H^2} \right) + f(i,j) \qquad 1.12$$

$$\left(\frac{\partial Q_g}{\partial x} \right)_{i,j} = \left(\frac{Q_g(i,j+1) - Q_g(i,j-1)}{2H} \right) m(i,j) \qquad 1.13$$

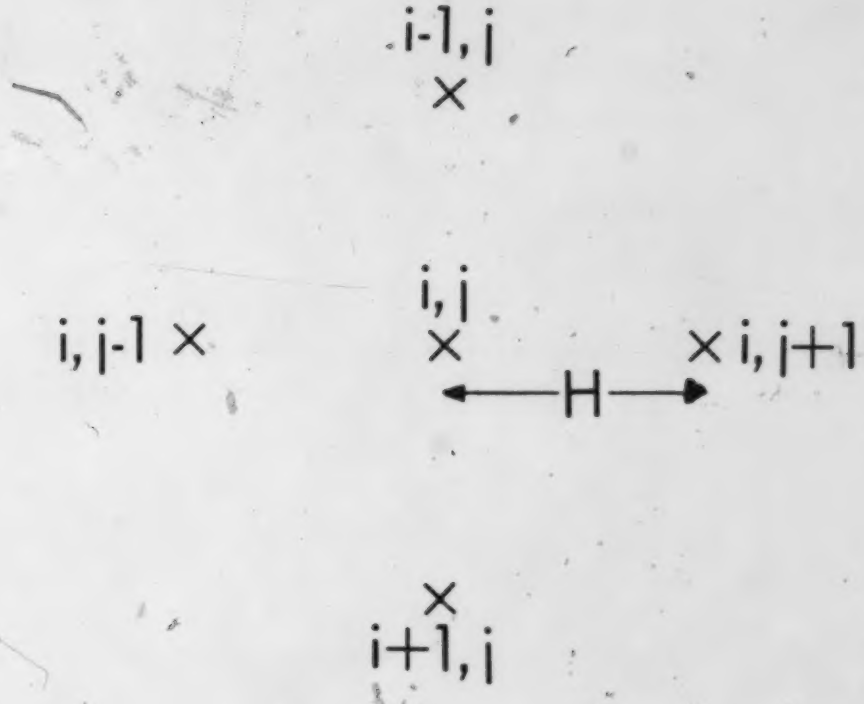

Fig. 4. Gridpoint (i, j) and four neighbouring gridpoints required for finite-difference terms in vorticity method of vertical velocity calculations.

$$\left(\frac{\partial Q_g}{\partial y}\right)_{i,j} = \left(\frac{Q_g(i+1,j) - Q_g(i-1,j)}{2H}\right) m(i,j) \qquad 1.14$$

$$\left(\frac{\partial Q_g}{\partial t}\right) = \frac{Q_{g(t+\Delta t)}(i,j) - Q_{g(t-\Delta t)}(i,j)}{2\Delta t} \qquad 1.15$$

where $Z(i,j)$ is the geopotential height of a pressure level at point (i, j),

$m(i,j) = \frac{1+\sin(60^\circ)}{1+\sin(\Psi)}$ is the map scale correction factor at latitude Ψ for the gridpoint (i, j) for a polar stereographic projection at 60°N.

$f(i,j)$ is the Coriolis parameter at gridpoint (i, j),

H is the grid spacing = 381 km.,

Δt is the time interval = 12 hours,

$Q_{g(t+\Delta t)}$ is the geostrophic vorticity at time $t+\Delta t$,

and $Q_{g(t-\Delta t)}$ is the geostrophic vorticity at time $t-\Delta t$.

1.4.3 Vertical Velocity: The Omega Equation:

The second method to be used in this study for calculating vertical velocities is the omega equation for a quasi-geostrophic system. Derivation of the equation follows that given by Haltiner (1971). The quasi-geostrophic vorticity equation for an (x,y,p,t) coordinate system is:

$$\frac{g}{\bar{f}}\nabla^2\frac{\partial Z}{\partial t}+\vec{V}\cdot\nabla Q=\bar{f}\frac{\partial w}{\partial p} \qquad 1.16$$

where $\bar{f}$ is the average Coriolis parameter over the area of interest.

The thermodynamic equation assuming no diabatic heat term is

$$\frac{\partial}{\partial t}\left(\frac{\partial Z}{\partial p}\right)+\vec{V}\cdot\nabla\frac{\partial Z}{\partial p}+\sigma w=0 \qquad 1.17$$

where $\sigma=\frac{1}{\theta}\frac{\partial Z}{\partial p}\frac{\partial \theta}{\partial p}$ is the static stability.

To eliminate the time derivatives in (1.16) and (1.17), differentiate (1.16) partially with respect to p and take the Laplacian of (1.17) and subtract the two resulting equations. The result of this manipulation is the omega equation.

$$\sigma\nabla^2 w+\frac{\bar{f}^2}{g}\frac{\partial^2 w}{\partial p^2}=\frac{\bar{f}}{g}\frac{\partial}{\partial p}(\vec{V}\cdot\nabla Q)-\nabla^2\left(\vec{V}\cdot\nabla\frac{\partial Z}{\partial p}\right) \qquad 1.18$$

The advection terms $\vec{V}\cdot\nabla Q$ and $\vec{V}\cdot\nabla\frac{\partial Z}{\partial p}$ may be written as:

$$\vec{V}\cdot\nabla Q=u\frac{\partial Q}{\partial x}+v\frac{\partial Q}{\partial y}=-\frac{g}{\bar{f}}\frac{\partial Z}{\partial y}\frac{\partial Q}{\partial x}+\frac{g}{\bar{f}}\frac{\partial Z}{\partial x}\frac{\partial Q}{\partial y}$$

using the quasi-geostrophic wind components $u=-\frac{g}{\bar{f}}\frac{\partial Z}{\partial y}$ and $v=\frac{g}{\bar{f}}\frac{\partial Z}{\partial x}$

$$\therefore \vec{V}\cdot\nabla Q=\frac{g}{\bar{f}}J(Z,Q)$$

where J is the Jacobian operator.

Similarly,

$$\vec{V}\cdot\nabla\frac{\partial Z}{\partial p} = J\left(Z, \frac{\partial Z}{\partial p}\right)$$

Thus, the omega equation may be written as:

$$\sigma\nabla^2\omega + \frac{f^2}{g}\frac{\partial^2\omega}{\partial p^2} = \frac{\partial}{\partial p}\left(J(Z,Q)\right) - \nabla^2\left(J\left(Z, \frac{\partial Z}{\partial p}\right)\right) \qquad 1.19$$

In order to solve this equation numerically, finite-difference forms of all derivatives in (1.19) must be used. The horizontal grid is identical to that used for the vorticity method, as shown in Figure 3, except that, for the omega equation, the dimensions were increased to 20 x 20 by adding 4 gridpoints to all sides of the 12 x 12 grid.

Figure 5 shows a central gridpoint (i, j) and its eight neighbouring gridpoints, as used in the horizontal finite-difference approximations. The two horizontal operators are the Laplacian and the Jacobian.

(i) The Laplacian:

The finite-difference form of the Laplacian of a quantity Z evaluated at a point (i, j) is:

$$\nabla^2 Z(i,j) = \left(\frac{Z(i,j-1)+Z(i,j+1)+Z(i-1,j)+Z(i+1,j)-4Z(i,j)}{H^2}\right)m(i,j)^2 \qquad 1.20$$

where ∇^2 refers to the finite-difference form of the Laplacian.

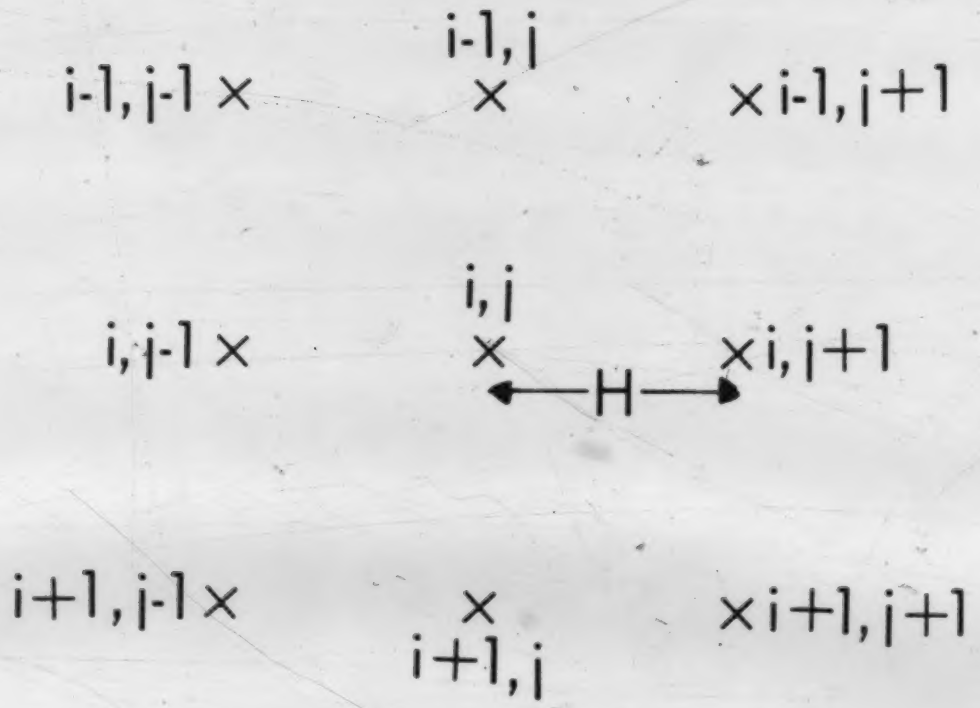

Fig. 5. Gridpoint (i,j) and eight neighbouring gridpoints used in finite-difference terms for the omega equation.

(ii) The Jacobian:

The general definition of the Jacobian of two variables A and B is:

$$J(A,B) = \frac{\partial A}{\partial x}\frac{\partial B}{\partial y} - \frac{\partial B}{\partial x}\frac{\partial A}{\partial y}$$

The finite difference form of the Jacobian at point (i, j) is:

$$J(A,B)(i,j) = \frac{m(i,j)^2}{4H^2}\left[\left(A(i,j+1)-A(i,j-1)\right)\left(B(i-1,j)-B(i+1,j)\right) - \left(A(i-1,j)-A(i+1,j)\right)\left(B(i,j+1)-B(i,j-1)\right)\right] \qquad 1.21$$

1.4.4 Vertical Structure for Omega Equation:

Figure 6 shows the isobaric levels required for the omega equation solution. The levels indicated by $Z(1)\cdots Z(4)$ are the levels at which the geopotential heights are used to solve for the ω's at the intermediate levels of 775 mb., 600 mb., and 400 mb. The lower (1000 mb.) and the upper (200 mb.) boundary ω- values are set to zero.

The finite-difference equation for the first derivative with respect to p, for a quantity ω, using the vertical indexing as in Figure 6 evaluated at say level 2 (775 mb.) is the following:

$$\left(\frac{\partial \omega}{\partial p}\right)_2 = \frac{\omega(1)-\omega(3)}{p(1)-p(3)} \qquad 1.22$$

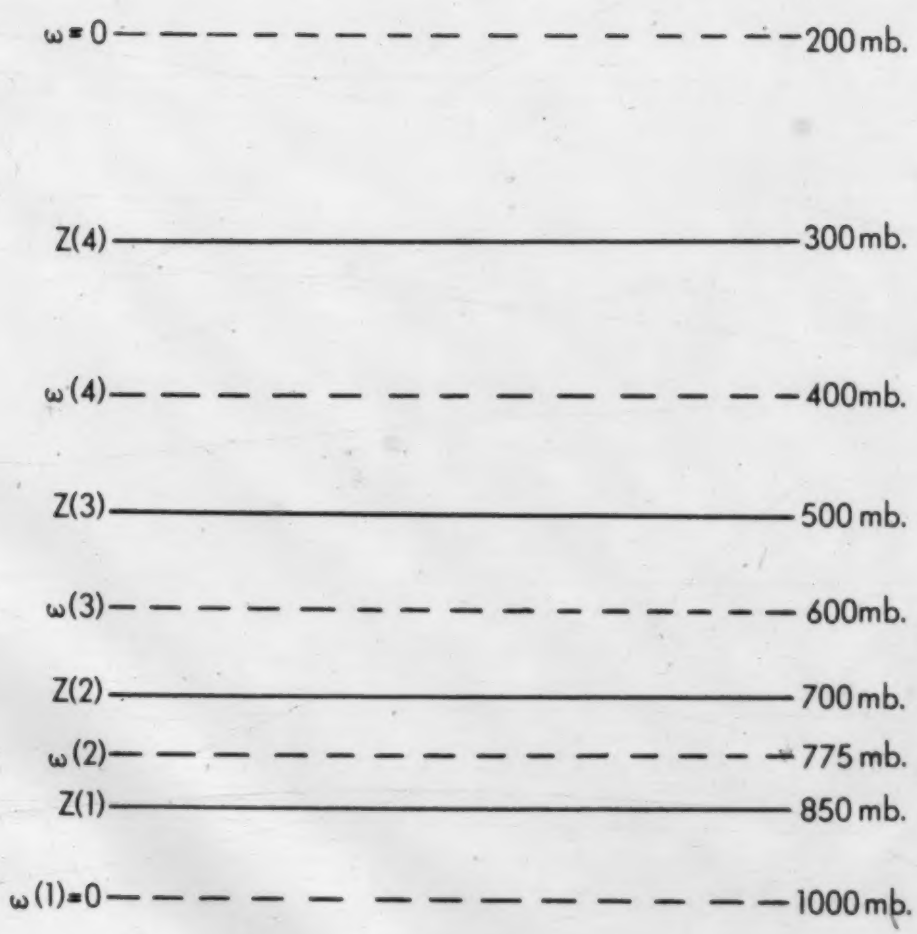

Fig. 6. Vertical structure for omega equation solution.

where the subscript 2 refers to the $\frac{\partial w}{\partial p}$ evaluated at level 2 (775 mb.).

The second derivative with respect to p at level 2 (775 mb.) is given by the following expression:

$$\left(\frac{\partial^2 w}{\partial p^2}\right)_2 = \frac{\left[\frac{w(1)-w(2)}{p(1)-p(2)}\right]-\left[\frac{w(2)-w(3)}{p(2)-p(3)}\right]}{\frac{p(1)+p(2)}{2}-\frac{p(2)+p(3)}{2}} \qquad 1.23$$

1.4.5 Omega Equation Solution:

The computer program used for the omega equation solution was written by Schram (1974) and modified by Hume (1975). Since the omega equation involves the Laplacian of a Jacobian term, the equation may be solved only at the inner 16 x 16 gridpoints. The solution for the equation was obtained by a relaxation procedure. This involves setting all gridpoints to a first-guess omega field, and then calculating at each gridpoint a residual which is the difference between the finite difference values of the left and right side of equation (1.19). If this residual is larger than a preassigned tolerance limit, then a correction is applied to that gridpoint by adding to it a fraction of the residual. The entire 16 x 16 grid is scanned in this manner, beginning at the lowest level at which ω is to be calculated i.e. 775 mb. and

ending at the uppermost level, namely 400 mb. After each complete scan, the number of times that the residual exceeds the tolerance limit is recorded. When this number is less than a prescribed constant (in this case 15), the scanning procedure is halted and the current ω -field becomes the final solution.

As previously indicated, the vertical velocities at the lower boundary (1000mb.) and the upper boundary (200 mb.) were set to zero. The lateral boundary gridpoints (the outer two gridpoints around the entire 20 x 20 grid) were set to initial first-guess omega values; these values were left unchanged throughout the subsequent relaxation process.

The static stability used in the omega equation was calculated from the following:

$$\sigma = \frac{1}{\theta}\frac{\partial z}{\partial p}\frac{\partial \theta}{\partial p}$$

$$= \frac{RT}{p\theta}\frac{\partial \theta}{\partial p} \qquad 1.24$$

where $\frac{\partial z}{\partial p} = -\frac{1}{g\rho}$ and $\rho = \frac{p}{RT}$, from the hydrostatic equation and the equation of state respectively. The static stability was calculated at 775 mb., 600 mb., and 400 mb. from the U.S. Standard atmosphere values for T and θ , as tabulated by Hess (1959). The σ -values at each pressure level were left constant

at all points on the grid. Haltiner et al (1963) have calculated vertical velocities from the omega equation using three different methods of obtaining static stabilities. The first method is to use a single static stability, which is the average of all σ-values calculated at all gridpoints and at all pressures concerned. The second method involves a σ-value which is a function of pressure only, and is the average of σ-values calculated over the grid at each pressure level. The third method makes use of σ-values which varied horizontally and vertically. Haltiner et al found that the vertical velocities varied by only about 10 percent in the lower levels, but by larger amounts at the higher levels. Thus, the variations in omega values due to the static stability variability are relatively small, so that the use of a constant static stability, at each pressure level, as calculated from the U.S. Standard Atmosphere appears justified.

1.5 Statistical Treatment of the Results

Several distributions of moisture and temperature parameters are presented in Chapter III. The statistical calculations that were used are described in the following subsections. Brooks et al (1953) is the

source for the following definitions.

(1) Mean:

The mean is defined as:

$$\bar{x} = 1/n \sum_{i=1}^{n} x_i \qquad 1.25$$

where x_i are the sample values,

and n is the number of observations in the sample.

(2) Mode:

The mode is defined as the most frequently occurring value of the variable.

(3) Median:

The median is defined as the value of the variable above and below which one half of the observations occur.

(4) Moments:

The general definition of the kth. moment is given by:

$$\mu_k = \frac{1}{n} \sum_{i=1}^{n} (x_i - \bar{x})^k \qquad 1.26$$

(5) Skewness:

The skewness of a distribution is the measure of the departure from symmetry of a frequency distribution. If the mode of the distribution falls to the left of the mean, the skewness is positive while if the mode falls to the right of the mean, the skewness is negative.

The mathematical expression for skewness is:

$$\gamma_1 = \mu_3 / \mu_2^{3/2} \qquad 1.27$$

(6) Kurtosis:

Kurtosis is a distortion from symmetry of the distribution which occurs when a disproportionately large or small number of observations occur in the ranges between the mean and the extreme values of the distribution. In the former case, the distribution is "platykurtic" while in the latter case it is "leptokurtic." The mathematical expression for kurtosis is:

$$\gamma_2 = \frac{\mu_4}{(\mu_2)^2} - 3. \qquad 1.28$$

When $\gamma_2 > 0$, the distribution is "leptokurtic" while when $\gamma_2 < 0$, the distribution is "platykurtic." Figure 7 shows schematic distributions illustrating skewness and kurtosis.

(7) "Log-Normal" Transformation:

Brooks et al (1953) discuss a method of transforming a variable which is not normally distributed into a variable which is more normally distributed. The transformation is called "log-normal" and may be used when a distribution has a positive skew and is leptokurtic, so that γ_1 as given by equation (1.27)

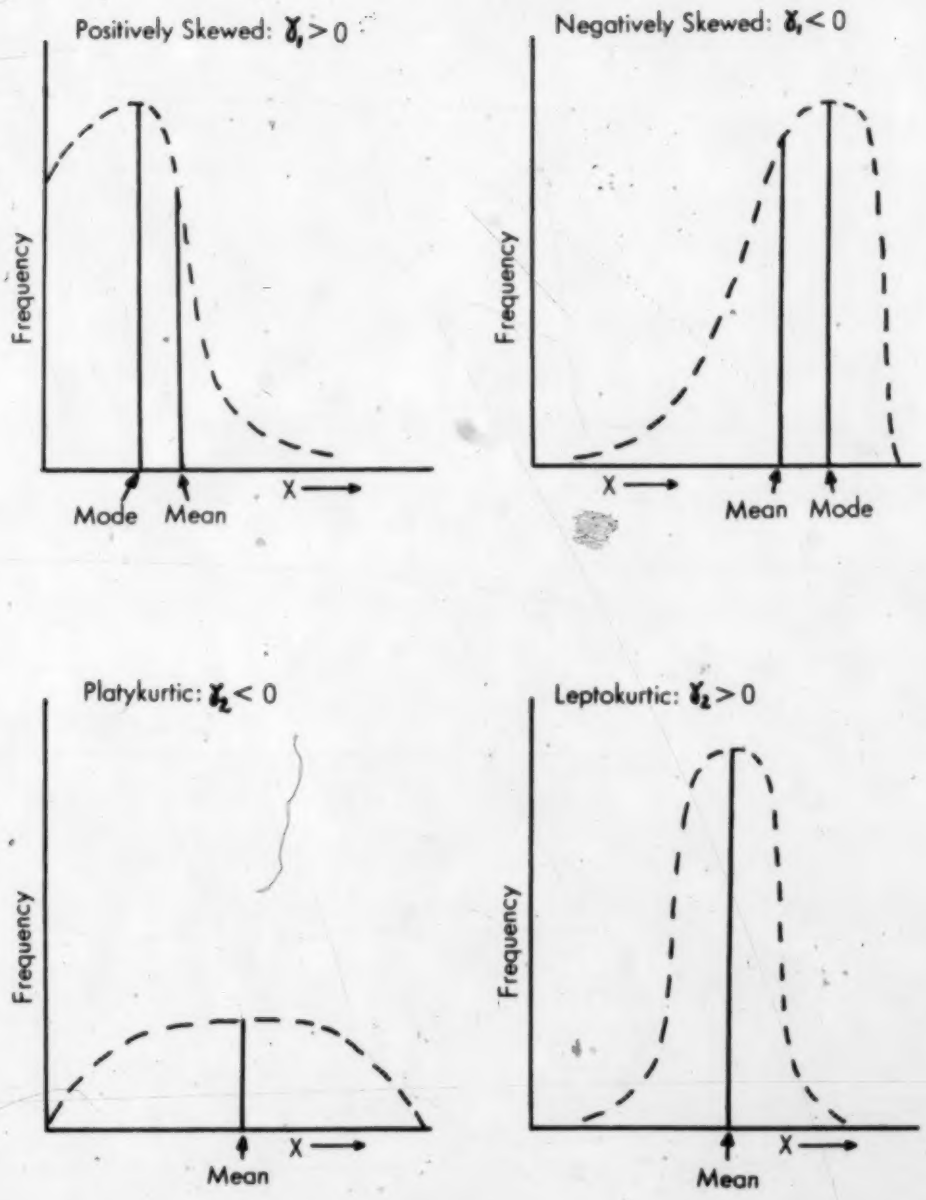

Fig. 7. Schematic diagrams to illustrate skewness and kurtosis.

and γ_2 as given by equation (1.28) are both positive. An example of this transformation is given in Appendix A.

The form of the transformation is:

$$u = a + b\ln((x-\bar{x})+c)) \qquad 1.29$$

where a, b, c are constants,

u is the transformed variable,

x is the original variable,

and $\bar{x}$ is the mean of the original variable.

To fit the original distribution of $(x-\bar{x})$, the value of $\left(\frac{u-\bar{u}}{\sigma_u}\right)$ must be found for each $(x-\bar{x})$, where $\bar{u}$ is the mean of u and σ_u is the standard deviation of u. In order to obtain $\left(\frac{u-\bar{u}}{\sigma_u}\right)$ from the original distribution of $(x-\bar{x})$, the results of Finney (1941) may be used.

$$\left(\frac{u-\bar{u}}{\sigma_u}\right) = \frac{1}{\sigma_u}\left[\ln\left(1+\frac{\omega(x-\bar{x})}{\sigma_x}\right)+\frac{\sigma_u^2}{2}\right] \qquad 1.30$$

$$\omega = \left[\frac{1}{2}\gamma_1 + \sqrt{\frac{1}{4}\gamma_1^2+1}\right]^{1/3} + \left[\frac{1}{2}\gamma_1 - \sqrt{\frac{1}{4}\gamma_1^2+1}\right]^{1/3} \qquad 1.31$$

$$\sigma_u^2 = \ln(1+\omega^2) \qquad 1.32$$

where σ_x is the standard deviation of the original distribution of x,

γ_1 is the skew of the original distribution of x.

The procedure involved to obtain the transformation of x to $\left(\frac{u-\bar{u}}{\sigma_u}\right)$ is the following.

(a) Calculate γ_1 and γ_2 to determine whether they are both positive and hence if the "log-normal" transformation may be applied.

(b) Calculate σ_x and ω for the distribution of x.

(c) Calculate σ_u from equation (1.32).

(d) Calculate $\left(\frac{\mu-\bar{u}}{\sigma_u}\right)$ from equation (1.30).

Using the values of $\left(\frac{\mu-\bar{u}}{\sigma_u}\right)$ obtained by the above procedure, a table of probability integrals for the normal frequency curve such as Appendix II (c) of Brooks et al (1953) may be used to obtain the frequency distribution of $\left(\frac{\mu-\bar{u}}{\sigma_u}\right)$.

"Log-normal" distributions are particularly useful in statistical treatment of daily rainfall data.

CHAPTER II

SOURCES AND METHODS OF OBSERVATIONS

The sources of data and the manipulations required to process the data for the first three parts of this study are considered below. The maps required for the case study are described in Chapter IV.

2.1 500-mb. Cyclone Tracks

The first objective of this study was the determination of the monthly 500-mb. cyclone tracks over the Arctic areas for a period of one year, from June, 1973 to May, 1974. The charts used for this purpose were the 500-mb. height and thickness analyses issued by the Canadian Meteorological Centre (C.M.C.) daily at 0000 Z and 1200 Z (Greenwich Mean Time). The criteria used when recording the track of a 500-mb. low are the following.

(i) The low centre was labelled as such on the C.M.C. 500-mb. charts.

(ii) The low persisted for at least three consecutive twelve-hour periods.

(iii) The centre of the low was north of 60°N, and between approximately 40°W and 180°W, longitude. Over

the Arctic Ocean, this rule was modified to the extent that the centre, in order to qualify, needed to be within 350 to 400 nautical miles of the nearest radiosonde station.

The 500-mb. cyclone tracks for this period are shown in Figures 8 to 13. Since the period of study is only a single year, generalizations concerning the seasonal or monthly variations in position, frequency and persistence of these systems are not warranted. However, a few specific observations concerning the year under study may be made. Although the overall motion of the majority of cyclones was from west to east, the paths followed by individual systems frequently appeared to be erratic or at least complex. This complexity may in part simply reflect the sparseness of data. Thus, the path of a low may appear to loop, while the centre has actually moved in a relatively uniform manner. An example of such a questionable looping movement occurred between 02/1200 Z and 03/1200 Z, June, 1973 in the vicinity of 78°N, 90°W. Since this happened over such a short period and the loop was very small, it is difficult to say whether looping is real or fictitious, i.e. a consequence of the inherent uncertainties in the 500-mb. analysis. However, in some cases, looping or erratic motion is

so persistent that the complicated trajectory is probably genuine. An example is the low of 13/1200 Z to 31/1200 Z, April, 1974 whose path underwent several reversals in direction within a period of over two weeks.

It came as a surprise to find that so few tracks affected the Yukon-Mackenzie River- Great Slave Lake-Great Bear Lake areas in the 12-month period analysed. To determine whether this is typical would require examination of at least ten more years of data.

2.2 Selected Cases of 500-mb. Cyclone Tracks for Moisture and Temperature Analysis

For the second part of the study, 500-mb. cyclone tracks were chosen from the months of July, August and September, 1973. The lows chosen were required to have 500-mb. positions relatively close to upper-air observing stations in order that observations of cloud associated with the disturbance would be available as well. Another requirement was that the 500-mb. system selected for study was the dominant cyclone disturbance affecting the Canadian Arctic for the duration of a specific case study. Table I below lists the dates of 500-mb. cyclone tracks chosen for further study. Plots of these tracks were previously presented in Figures 8 and 9.

Table I

500 mb. low cases chosen for moisture and temperature analysis using satellite photographs

Case Number	Date, Time G.M.T.
1	06/0000Z-07/0000Z, July
2	09/1200Z-14/0000Z, July
3	19/0000Z, July-02/1200Z, August
4	10/0000Z-11/0000Z, August
5	13/1200Z, August
6	18/0000Z-24/1200Z, August
7	13/1200Z-17/1200Z, September
8	26/1200Z-29/0000Z, September

Fig. 8. 500-mb. cyclone tracks for June, July 1973.

June 1973

Several weak lows occurred. The strongest was 13/0000Z to 27/1200Z.

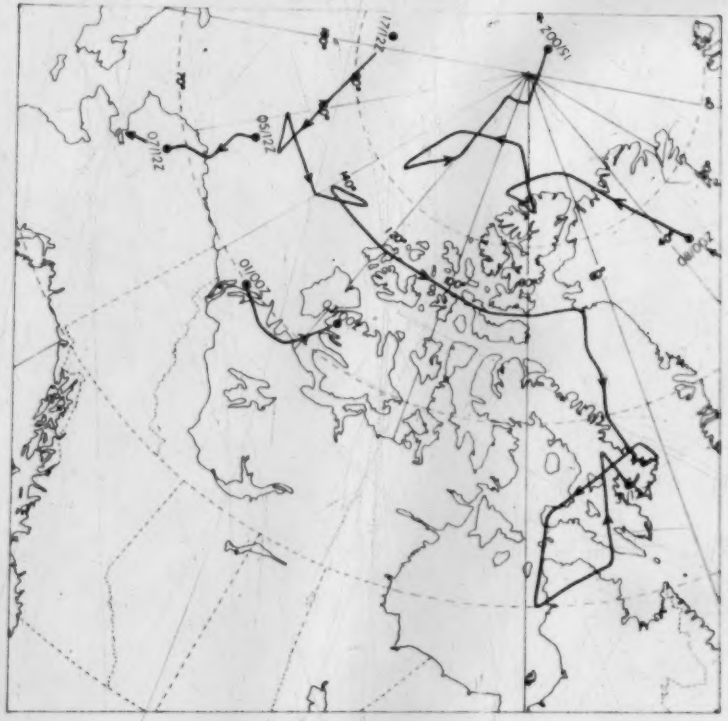

July 1973

The dominant low was 17/1200 Z to 31/1200 Z, to be studied in detail in Chapter III and in the case study of Chapter IV.

Fig. 9. 500-mb. cyclone tracks for August, September, 1973.

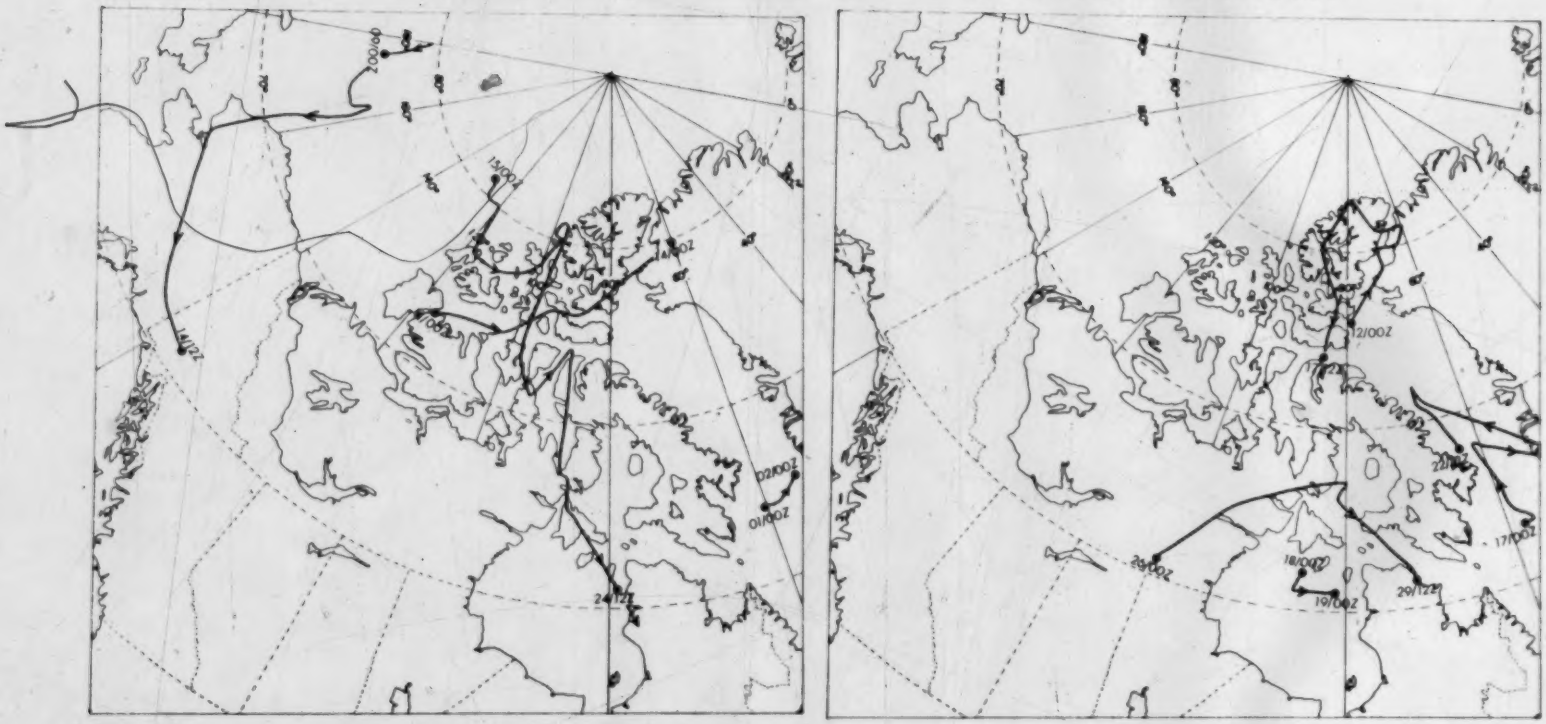

August 1973

September 1973

The strongest low was 15/0000 Z to 24/1200 Z.

Few, weak systems occurred.

Fig. 10. 500-mb. cyclone tracks for October, November, 1973.

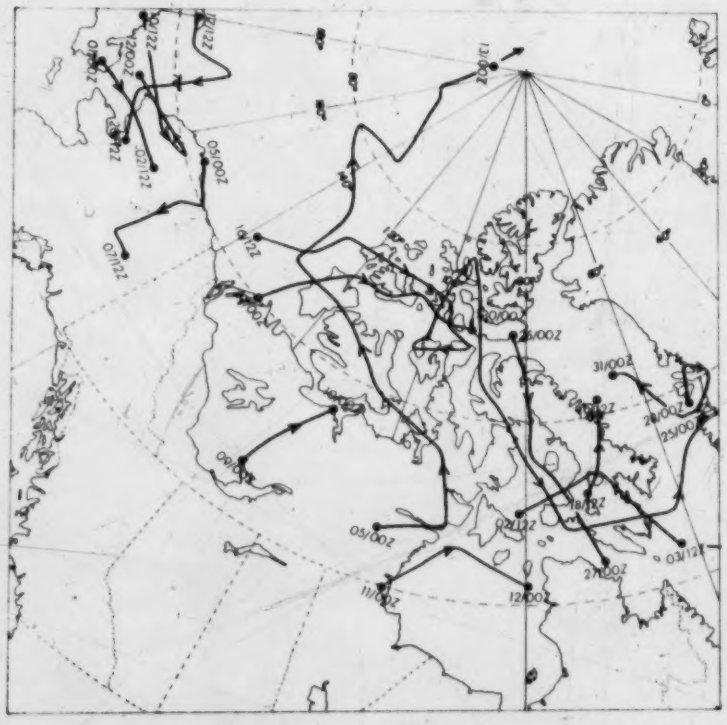

October 1973

02/1200 Z to 03/1200 Z and 05/0000 Z to 13/0000 Z lows were the most intense.

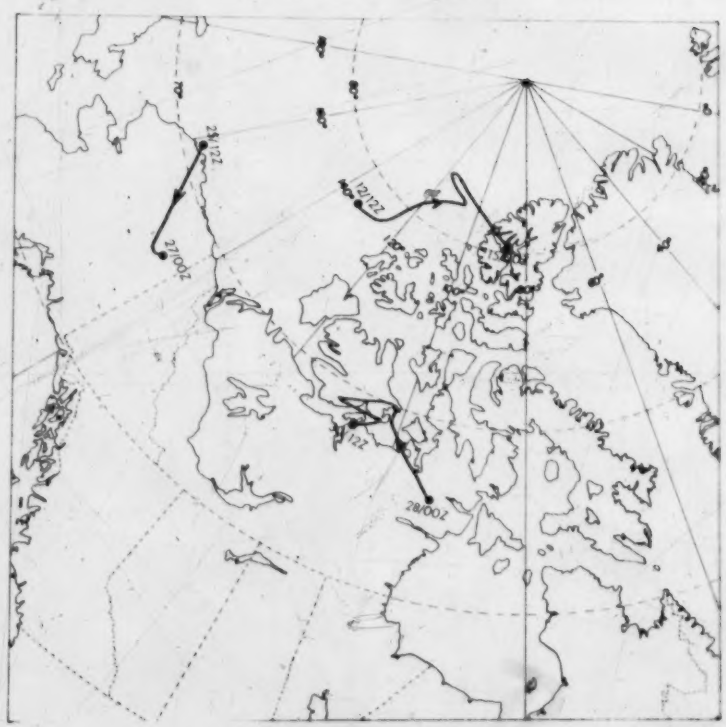

November 1973

An upper ridge dominated the circulation so that few lows occurred in the Arctic.

Fig. 11. 500-mb. cyclone tracks for December, 1973, January, 1974.

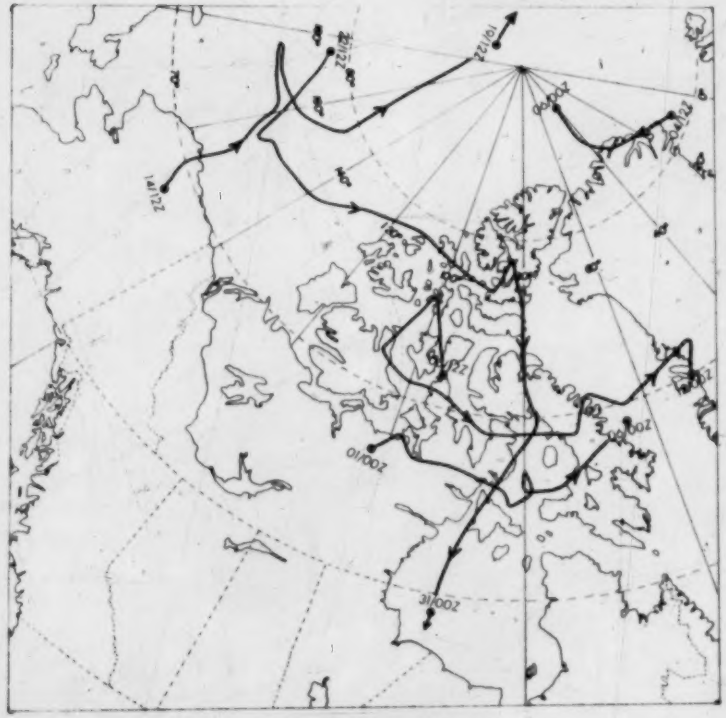

December 1973

The dominant systems were 05/1200 Z to 12/0000 Z and 22/1200 Z to 31/0000 Z.

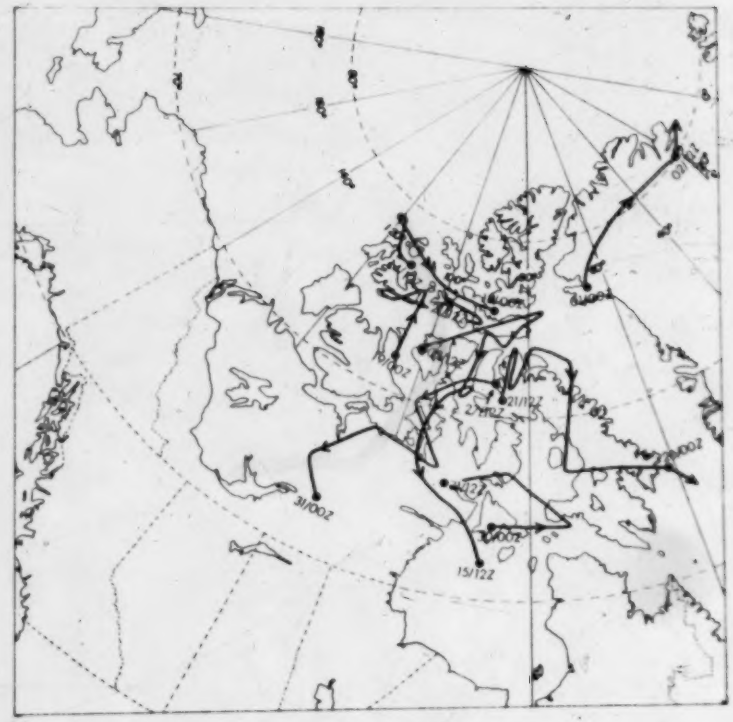

January 1974

The strongest cyclones were 03/1200 Z to 15/1200 Z and 27/1200 Z to 31/0000 Z.

Fig. 12. 500-mb. cyclone tracks for February, March, 1974.

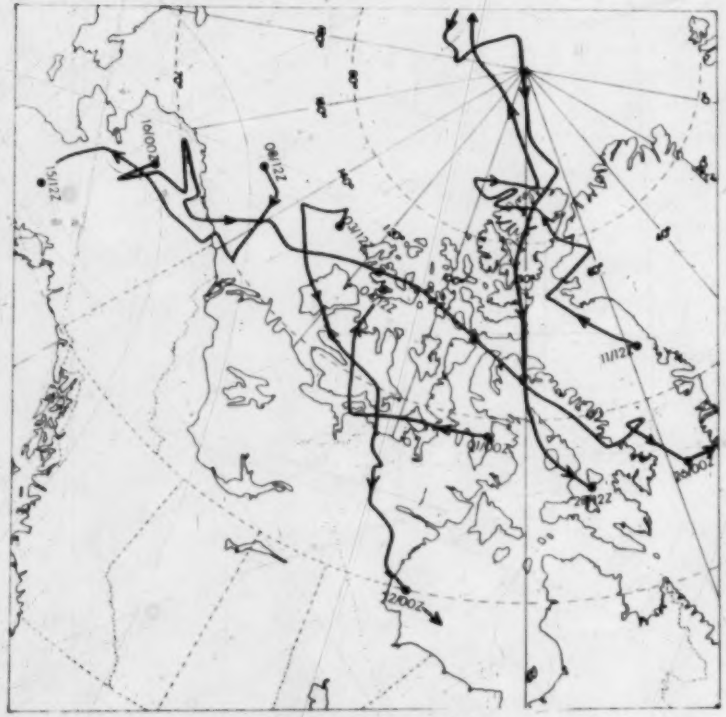

February 1974

The long, looping path of the 11/1200 Z to 28/1200 Z was the most interesting.

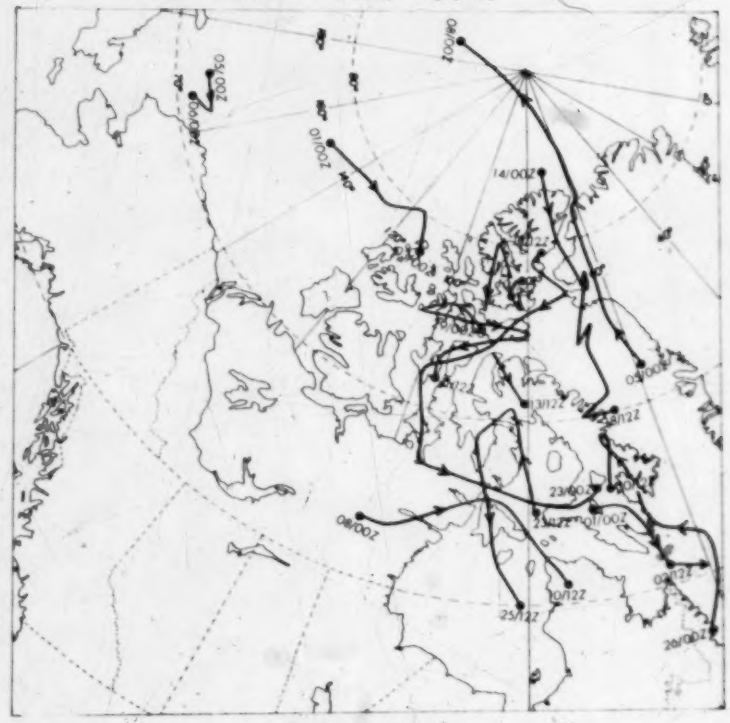

March 1974

Most lows were brief and weak except the 14/0000 Z to 18/1200 Z and 18/1200 Z to 23/0000 Z tracks.

Fig. 13. 500-mb. cyclone tracks for April, May, 1974.

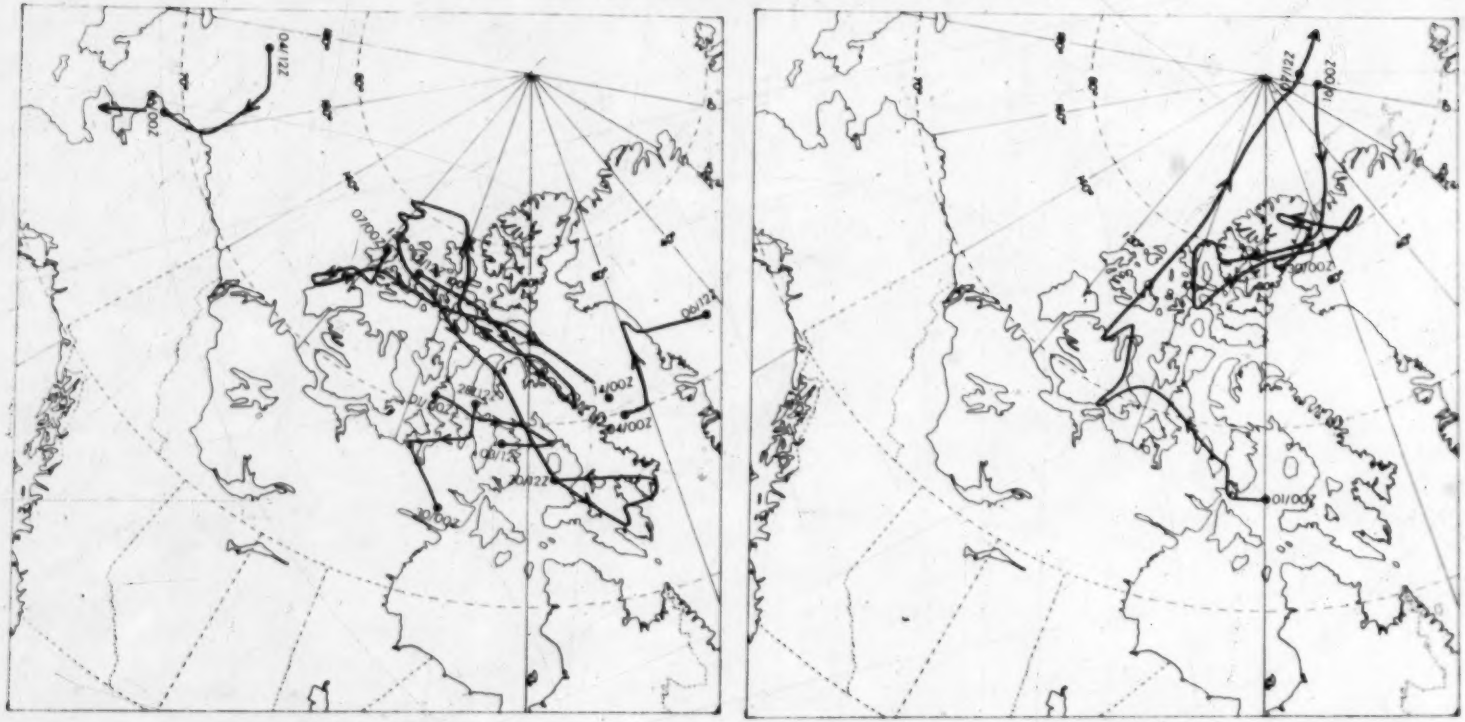

April 1974 May 1974

Few, but intense, 500-mb. cyclones occurred with the strongest and most erratic being from 13/1200 Z, April, 1974 to 07/1200 Z, May, 1974.

The cloud band model, used in the analysis of the temperature and moisture distributions of the cases listed in Table I, was adapted from a model devised by Shenk and Brooks (1965). They investigated the distribution of several cloud parameters associated with extratropical vortices in all seasons, and for three classifications of vortex development: developing, mature and dissipating. In the present study, no seasonal or vortex development separations are made. The model used is shown in Figure 14 below. The various regions shown in the diagram are defined and labelled with letters, as follows:

(a) Area C:

This classification includes all cloud areas around the vortex centre. The areas may or may not be organized in bands. For each cloud observation, a further classification as to low, C(L) or middle, C(M) cloud types was made according to the criteria set out in Chapter I. The limitation on the cloud associated with a given vortex centre was subjectively set as the edge of the cyclonic circulation around the 500-mb. low centre.

(b) Area An:

This is the clear area located to the north of the vortex centre and north of the cloudmass C.

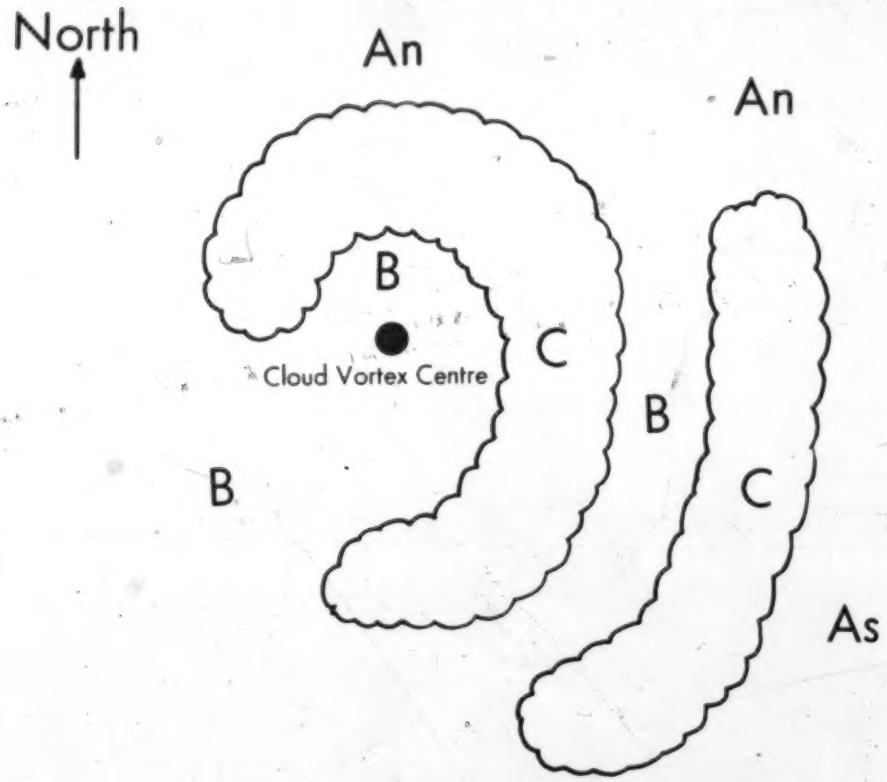

Fig. 14. Idealized cloud band model showing regions around vortex centre. Adapted from Shenk and Brooks (1965).

(c) Area As:

This is the clear area to the south of the vortex centre and also to the east of the cloudmass C.

(d) Area B:

This comprises the clear area, to the west of the cloudmass or between the cloud bands. It must lie to the south of the vortex centre if located to the west of the cloud mass. The exception to this is that if a cloudless area extends into the centre of the vortex and continues north of the centre, this area is then also classified a "B". For the clear area between cloud bands, the "B" classification applies in all cases, whether north or south of the vortex centre.

Figure 15 below shows a satellite image with several cloud areas classified according to the Shenk and Brooks model. A main cloud vortex centre appears near (1) in Baffin Bay, with a secondary centre near (2) over central Baffin Island. A double low-pressure centre is also evident on the surface analysis (not shown here) with cloud vortex (1) being close to the main surface low position and vortex (2) close to a weaker surface trough over Baffin Island. The 500-mb. chart, analyzed at 25/1200 Z, July (about four hours before the satellite image time) shows a

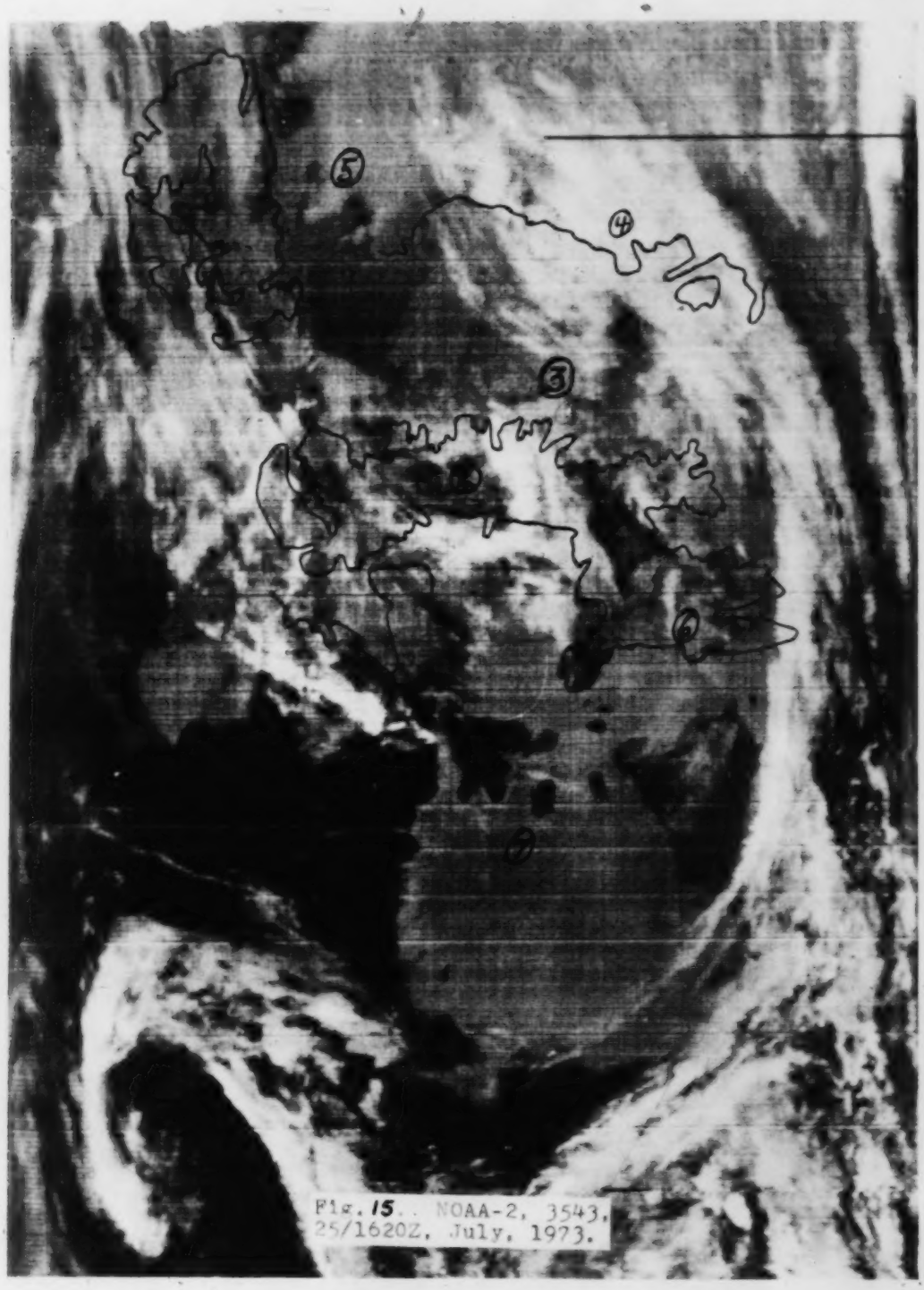

Fig. 15. NOAA-2, 3543, 25/1620Z, July, 1973.

500-mb. vortex centre at (3) in Figure 15 with a large cyclonic circulation covering the entire central and eastern Arctic regions. Following the cloud model, several areas are labelled on the satellite image. These are: (4) over western Greenland - middle cloud, C(M), around vortex centre; (5) over northern Greenland-clear area, An, to the north of the vortex centre and north of the cloudmass area (4); (6) over southern Baffin Island - low cloud area, C(L), around vortex; (7) over northern Hudson Bay - clear area, B, to the south of the vortex centre, and west of the cloudmass over northern Quebec.

In order to position each radiosonde station according to this model, an adjustment for the time between the cloud observation time and the radiosonde observation time had to be made. The reason for this is the following: at the time of the satellite pass, a cloud mass could have been present over the radiosonde station, so that the satellite image would show the station obscured by cloud. However, at the time of the upper-air observation, the station could have been in a clear area so that the conventional meteorological parameters recorded at the station would differ from those inferred from the satellite image. Corrections were made to compensate for this motion of the cloud area between

the time of the satellite photo and the upper-air observation time. The scheme used was to compute the speed and direction of motion of the 500-mb. low centre at the time when the satellite image was taken. This was done by using the low-centre positions at the nearest synoptic time periods before and after the photo time. Figure 16 shows a sketch of the adjustment procedure. In this example, the satellite image was taken at 12/2100 Z and the radiosonde observation was taken at 13/0000 Z. The speed and direction of motion of the 500-mb. low was determined by using the low-centre positions at synoptic times nearest the satellite photo observation time (here 12/1200 Z and 13/ 0000 Z). Then, the cloud-edge position was corrected by moving it in the direction of motion of the vortex centre by a distance equal to that covered by the vortex in the three-hour period between the satellite photo time and the time of the upper air observation. The new, corrected cloud-edge position is then the cloud position at the radiosonde observation time. Since the radiosonde observations are taken at twelve-hour intervals, this correction did not have to be applied for periods in excess of six hours.

On the basis of the 500-mb. low tracks recorded in Table I, 43 infrared images were chosen for analysis. A total of 216 radiosonde station soundings were classified

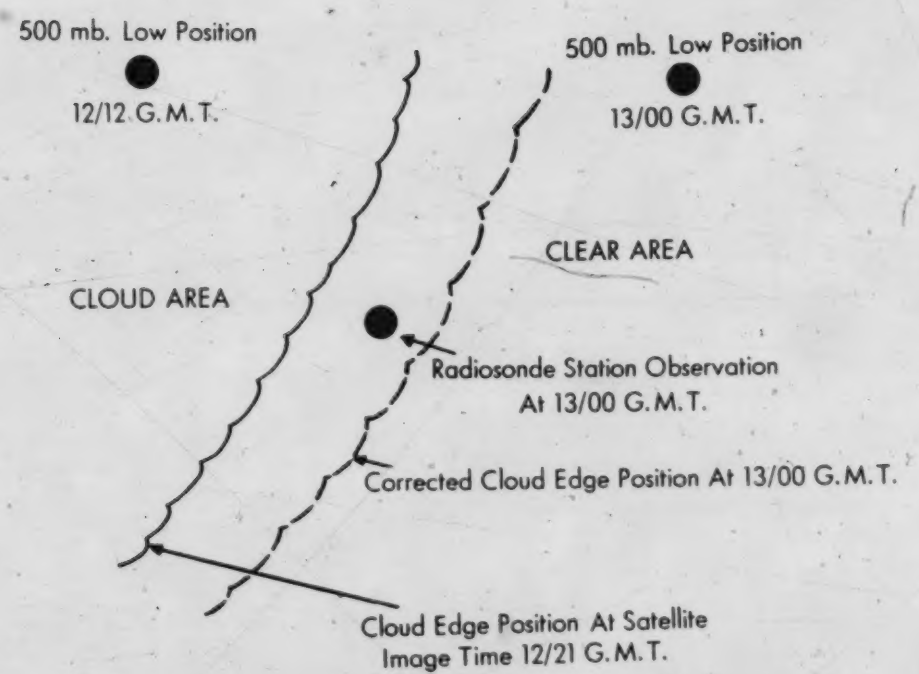

Fig. 16. Adjustment of cloud pattern for satellite photo-upper air observation time difference.

into low or middle cloud or clear areas, according to the cloud-band model described.

Dewpoint depressions were obtained from the C.M.C. surface, 850-mb. 700-mb. and 500-mb. analyses. Vertical temperature differences between the surface and 850 mb., 850 and 700 mb. and 700 and 500 mb. were also recorded.

A third field, the moisture thickness, was obtained from radiosonde data plotted routinely at the Arctic Weather Central, Edmonton Alberta. The moisture thickness at a given radiosonde station was calculated by totalling all layers, below approximately 450 mb., whose dewpoint depression was less than 5°C. The actual layer thicknesses were recorded using the tephigram pressure-level heights directly. It is realized that use of the tephigram to obtain the thickness in this manner introduces an error, since the pressure-level heights recorded on the tephigram are based on the U.S. Standard Atmosphere. An estimate of the error introduced by this was made by considering a 1000 to 500-mb. thickness of 5460 geopotential metres for the U.S. Standard Atmosphere. Examination of several of the C.M.C. thickness charts indicated a minimum thickness of about 5040 gpm. and a maximum thickness of about 5760 gpm. Thus, using the U.S. Standard Atmosphere thicknesses, moisture-layer thicknesses near the deepest 500-mb. lows are a maximum of about

8 percent too high, and a maximum of about 5 percent too low near the strongest 500-mb. ridges. These are maximum errors; the actual percentage errors are generally less.

Another error arises in estimating the thicknesses from the tephigrams when determining the limits of layers which have dewpoint depressions less than 5°C. Linear interpolation between the plotted dewpoint depressions is used to obtain the intermediate level at which the dewpoint depression is 5°C. The error in the layer thickness estimation caused by this interpolation is approximately ± 10mb. or ± 300 feet, depending on the pressure level at which the interpolation is done.

A fourth field, extracted from radiosonde data, was the minimum dewpoint depression. It is the lowest dewpoint depression of the tephigram plot up to about 20,000 feet above m.s.l., excluding the surface dewpoint depression.

2.3 Vertical Velocity Calculations

From the several cases considered in the previous analysis of moisture and temperature, the case of 19/0000 Z to 31/1200 Z, July, 1973 was chosen for a more detailed vertical velocity, moisture and cloud pattern analysis.

For the vertical velocity calculations using the vorticity method, the geopotential heights at 1000, 850, 700 and 300 mb. were required. The omega equation vertical velocities required only the height data at 850, 700, 500 and 300 mb. These data were obtained from a magnetic tape of gridpoint heights supplied by the Canadian Meteorological Centre, Montreal, Quebec. Since the grid used in this study is identical in orientation to that used by C.M.C., the gridpoint data from the tape were used directly as input for the vertical velocity programs.

CHAPTER III

MOISTURE, TEMPERATURE AND VERTICAL VELOCITY RESULTS

3.1 Moisture and Temperature Distributions Associated With 500-mb. Lows in Summer

3.1.1 Dewpoint Depressions

The dewpoint depression distributions are shown in the histograms of Figures 17 to 20. The mean, mode, median and the number of observations for each distribution are shown in Table II. The abscissa labels refer to the dewpoint depressions such that e.g. a bar at "$\frac{8}{9}$" represents the percentage of observations with a dewpoint depression of 8° or 9°C. The distributions are also labelled according to the cloud model described in Section 2.2. The C(L) and C(M) refer to low and middle cloud areas, respectively, while the An, As, B distribution denotes the combined clear areas.

3.1.2 Surface Dewpoint Depressions

Both the C(L) and C(M) areas have strong, positively-skew distributions, with the former having a slightly smaller mean. This appears reasonable, since some of the cloud areas could extend right to the surface. Moreover, precipitation falling from the low cloud

would also cause smaller surface dewpoint depressions. The individual clear-area distributions should be considered as tentative, because of the small sample sizes. The combined (An, As, B) clear area - a larger sample - has a considerable drier distribution (mean dewpoint depression: 6°C.) than the cloud categories. Since 1200 Z observations are included, some of the small surface dewpoint depressions in the clear areas may be caused by nocturnal radiation cooling.

3.1.3 850-mb. Dewpoint Depressions

Again, both the C(L) and C(M) distributions are more moist than the clear-area distributions. However, the C(L) distribution is slightly drier than the C(M) distribution. This is contrary to what one would expect, since the 850-mb. level would normally be considered most representative of low-cloud moisture. It is likely that some of the low cloud observations are fog or low stratus associated with the numerous open water areas of the summer Arctic. On such occasions, the cloud may not extend to the 850-mb. level and the dewpoint depressions at 850-mb. will be larger. The middle cloud moist distribution may be caused by cloud layers extending downward to the 850-mb. level. The clear areas have dry distributions with a mean dewpoint depression of 11.8°C.

Table II

Dewpoint depression statistics
for low, middle cloud and clear areas

Class	Mean	Mode	Median	No. of observations
		Surface		
C(L)	2.9	1.0	1.8	98
C(M)	3.4	1.0	1.8	72
An, As, B	6.0	4.0	4.0	46
		850 mb.		
C(L)	6.3	0.0	5.4	97
C(M)	4.5	0.0	1.9	72
An, As, B	11.8	12.0	11.3	46
		700 mb.		
C(L)	9.5	7.0	8.0	98
C(M)	5.0	1.0	2.2	71
An, As, B	13.1	10.0	11.4	45
		500 mb.		
C(L)	11.0	13.0	10.7	98
C(M)	8.6	5.0	7.1	71
An, As, B	14.0	13.0	12.8	46

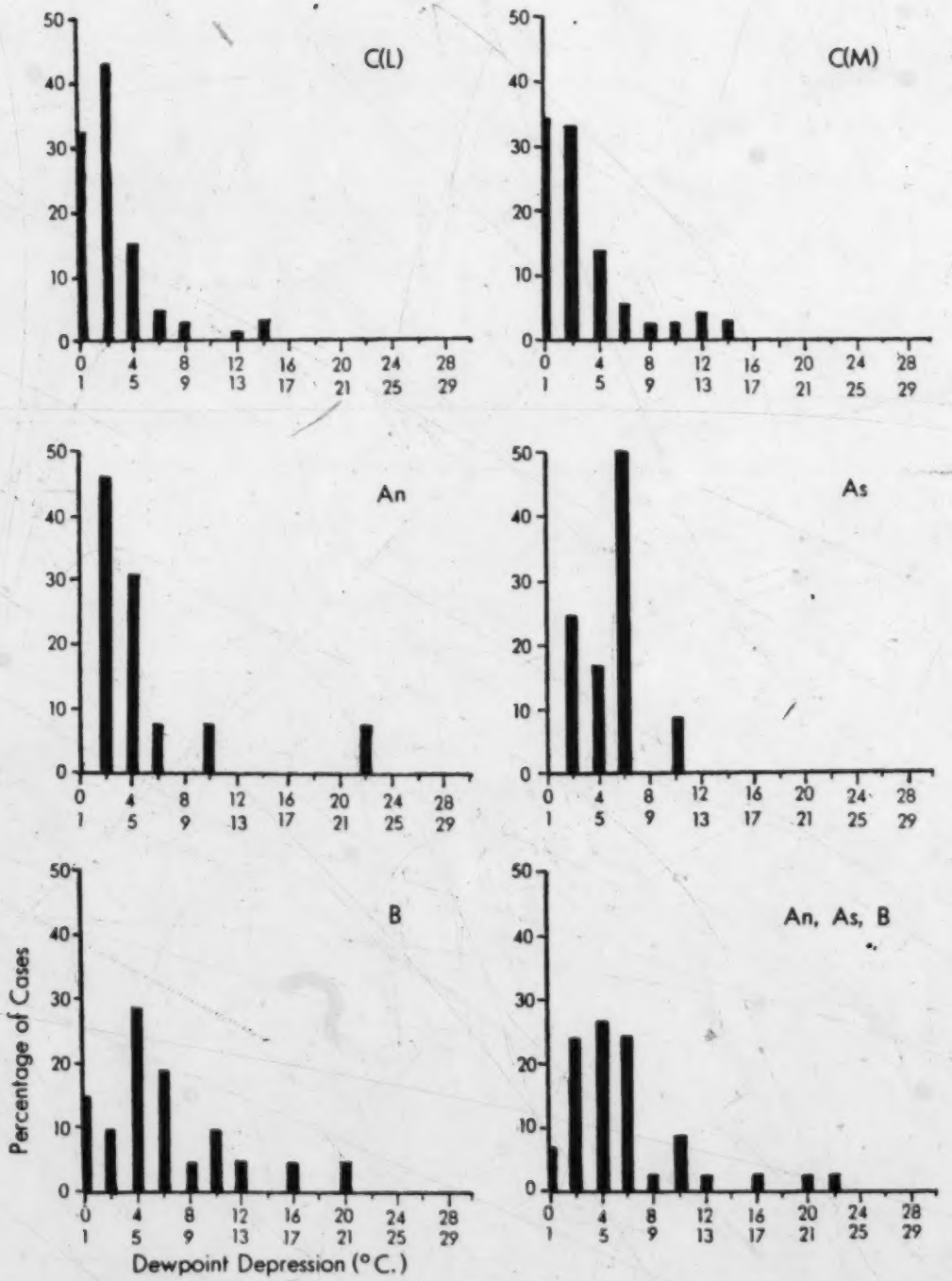

Fig. 17. Surface dewpoint depression distributions.

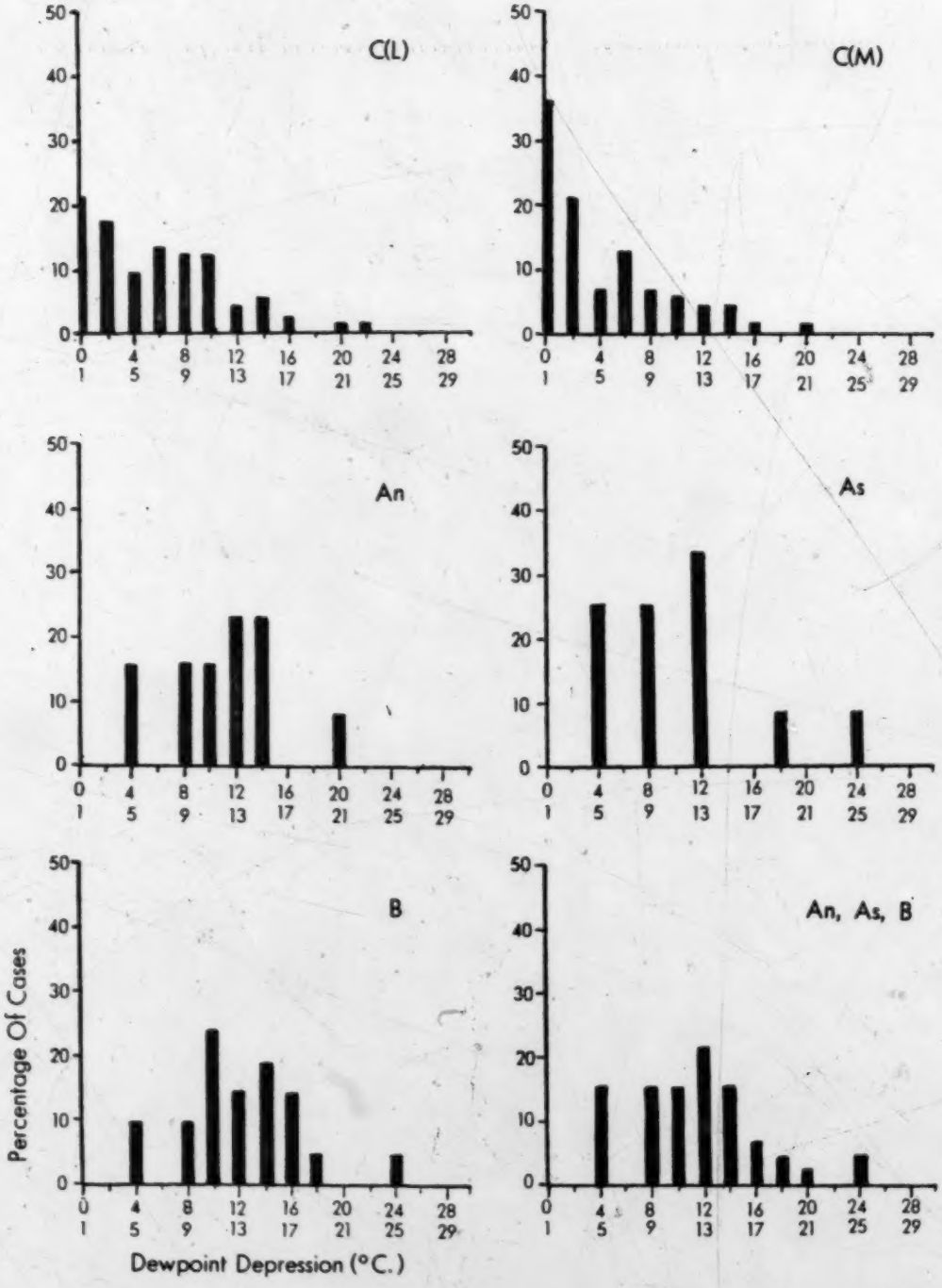

Fig. 18. 850-mb. dewpoint depression distributions.

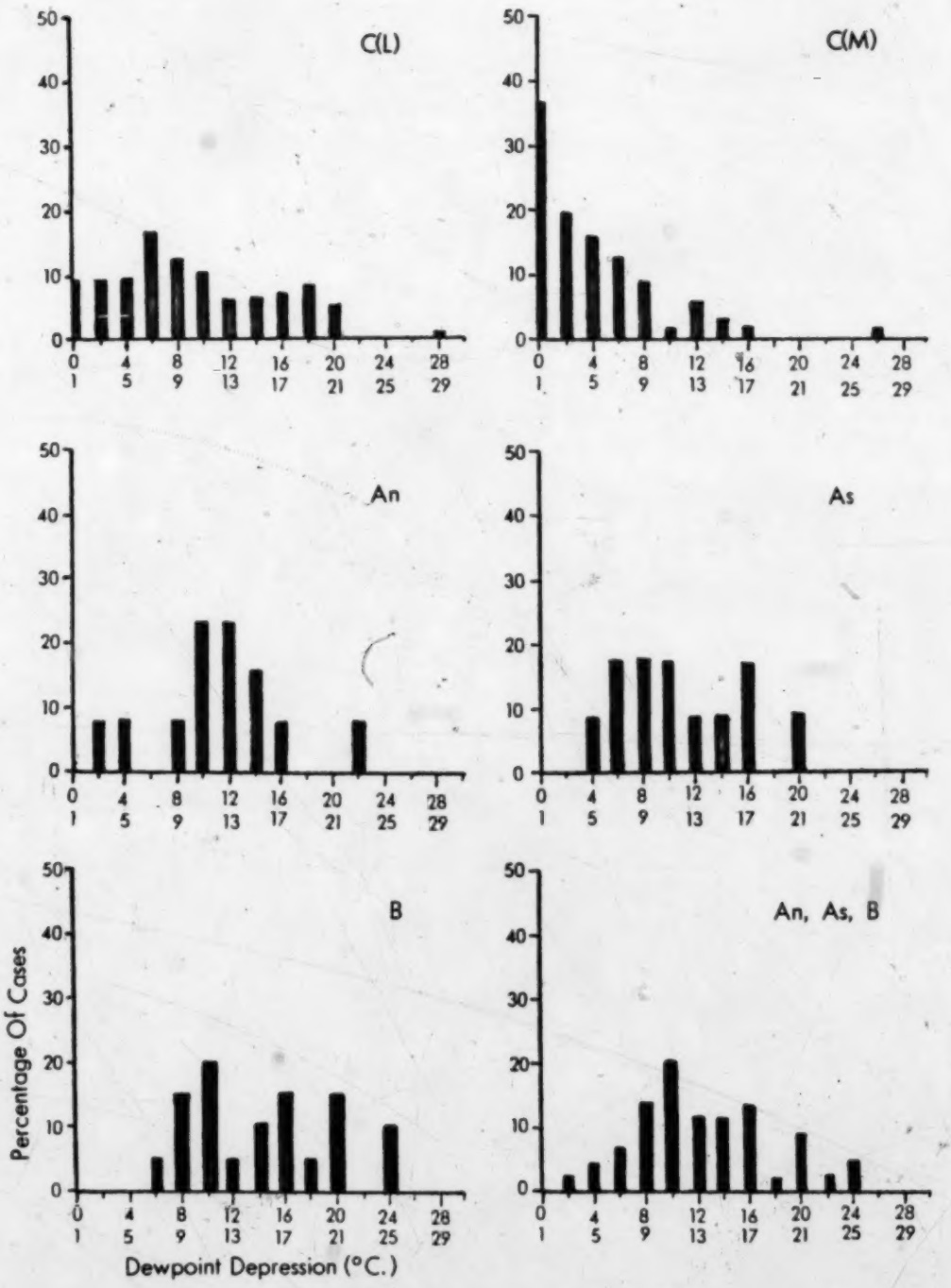

Fig. 19. 700-mb. dewpoint depression distributions.

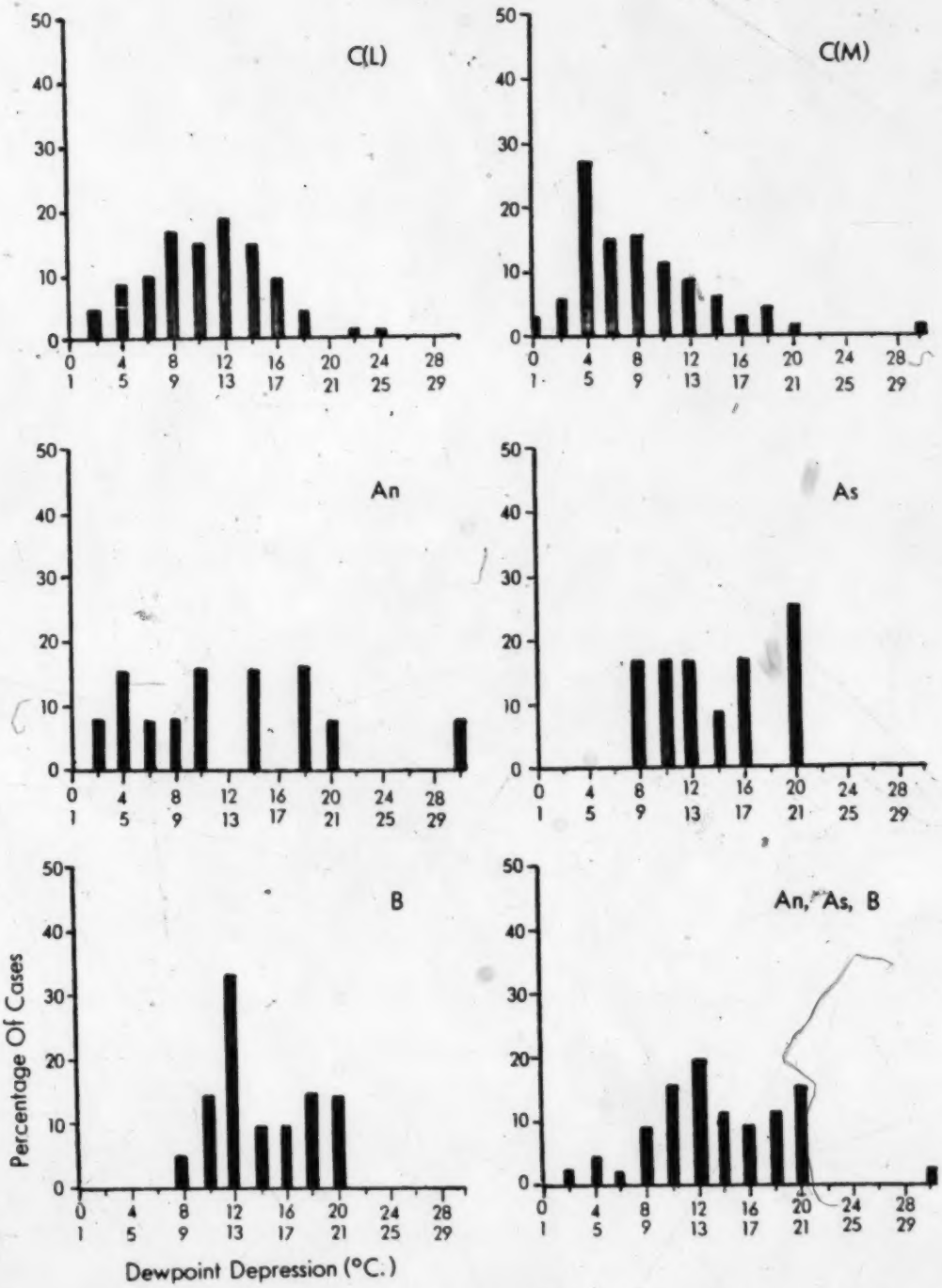

Fig. 20. 500-mb. dewpoint depression distributions.

3.1.4 700-mb. Dewpoint Depressions

The 700-mb. C(L) histogram shows widely distributed moisture. The observed pattern may be caused by moisture extending above the low cloud to the 700-mb. level. The saturated cases observed at 700-mb. in the C(L) areas could be simply the result of incorrect cloud type classification. Occasionally, a satellite image grey-shade was intermediate between the bright white of middle cloud and the darker shade of low cloud. Such a case could be wrongly classified as low instead of middle cloud. The moist C(M) distribution is to be expected, since 700-mb. is a representative level for middle-cloud analysis. Some 72 percent of the cases in the C(M) areas have dewpoint depressions $\leq 5^{\circ}C$. The clear distributions are again considerably drier, with a combined An, As and B mean of $13.1^{\circ}C$.

3.1.5 500-mb. Dewpoint Depressions

The 500-mb. level is frequently above the cloud layers. The C(M) area shows a significant percentage of cases with depressions $\leq 5^{\circ}C.$, probably caused by middle cloud extending to this level. The C(L) and clear areas are considerably drier.

3.1.6 Minimum Dewpoint Depressions

Figure 21 shows the minimum dewpoint depression distributions with the mean, mode and median in Table III. These results, obtained from tephigrams, are the minimum dewpoint depressions to approximately 20,000 feet M.S.L. The surface dewpoint depression was excluded since it may be unrepresentatively low for clear areas, at the 1200 Z observation, because of radiational cooling. The abscissa labels again indicate ranges of minimum dewpoint depressions, e.g. a bar at 2.5°C. denotes the percentage of cases with minimum dewpoint depression between 2.0°C. and 3.0°C.

The histograms show most cases in the C(L) and C(M) distributions in the 0.5°C. range. A considerable spread of minimum dewpoint depressions occurs with the clear areas.

3.1.7 Moist Layer Thicknesses

Moist-layer thickness distributions are shown in Figure 22; the corresponding means, modes and medians are given in Table III. Along the abscissa, a bar at "7" indicates the percentage of cases with a moist-layer thickness from 6000 to 8000 feet.

The majority of the C(L) cases are in the 3,5,7 ranges but some large moisture thicknesses also occur.

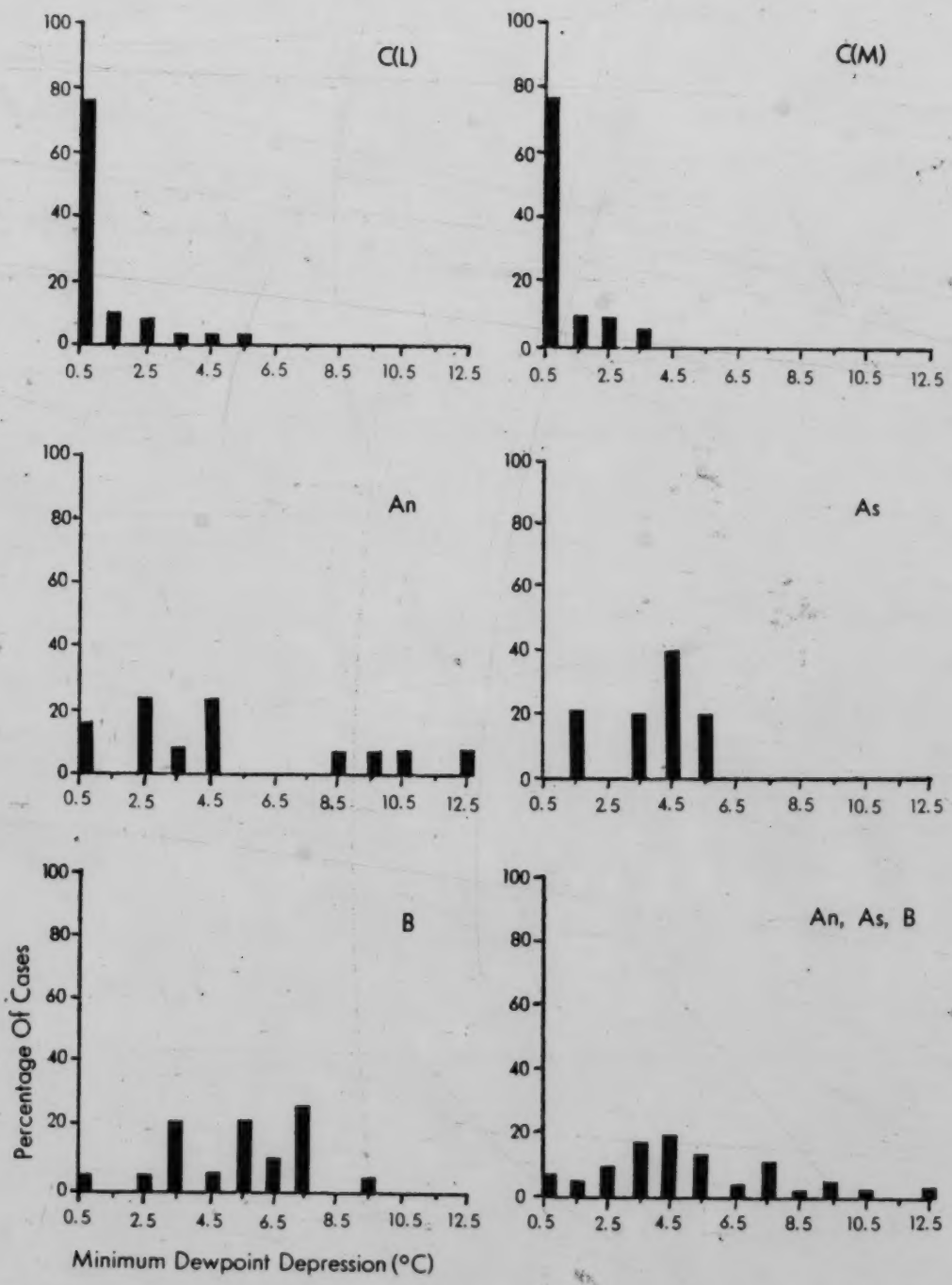

Fig. 21. Distributions of minimum dewpoint depressions above the surface and below 20000 ft.

Table III

Minimum dewpoint depression and moist layer statistics for low, middle cloud and clear areas

Class	Mean	Mode	Median	No. of observtions
		Minimum dewpoint depression (C.)		
C(L)	0.8	0.0-0.5	~0.4	95
C(M)	0.6	0.0-0.5	~0.4	64
An, As, B	4.8	4.5-5.0	~4.7	42
		Moist layer thickness (feet)		
C(L)	6695	4000 -5000	~ 4950	95
C(M)	11846	14000 -15000 19000 -20000	~ 13500	64
An, As, B	1332	0-1000	~ 750	42

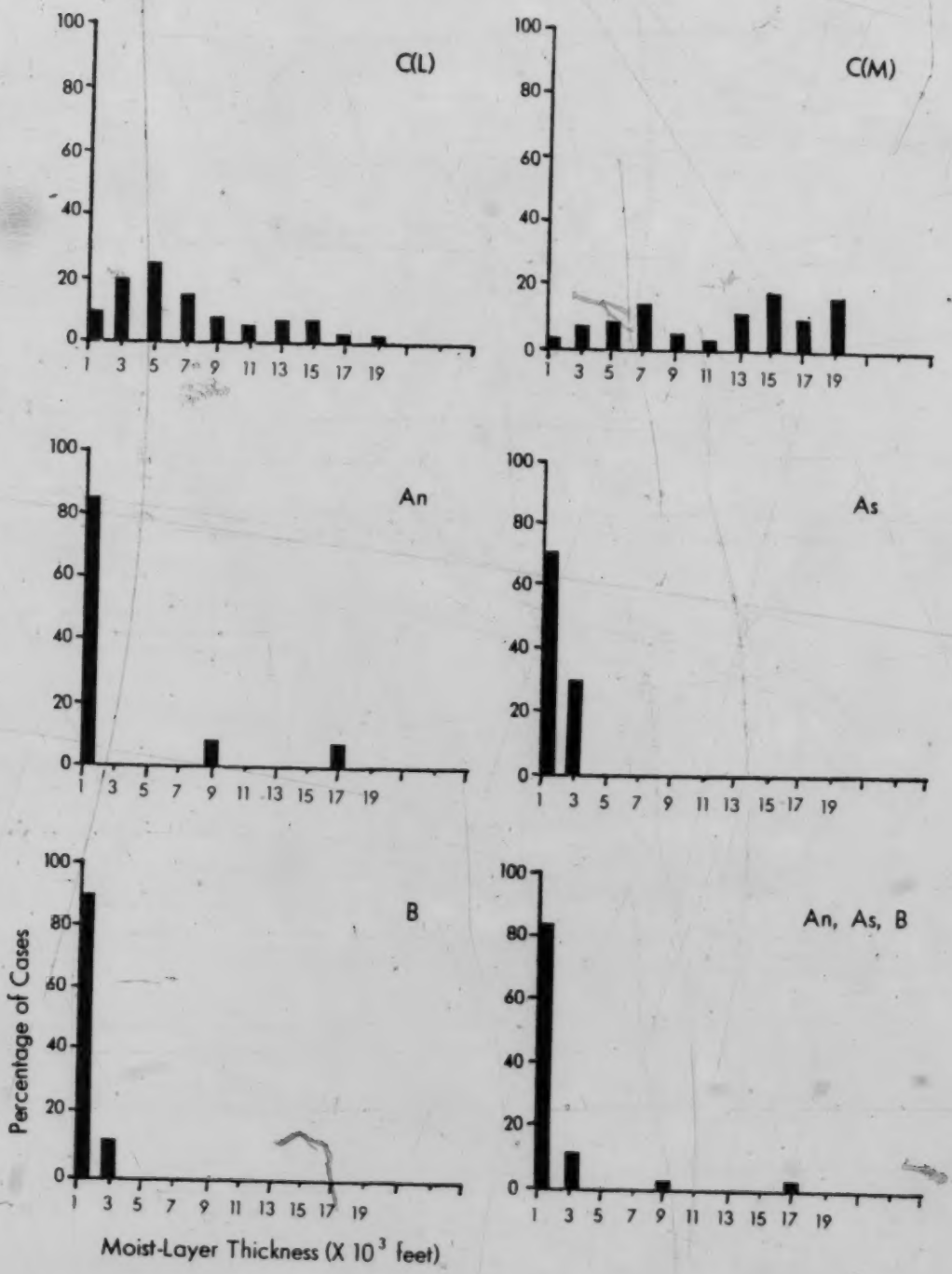

Fig. 22. Moist-layer thickness distributions.

Large-thickness cases are difficult to explain, since this would mean that some grey areas on the satellite image purporting to indicate low cloud have, on the basis of corresponding radiosonde data, much thicker moisture layers than expected. This could be due to errors in identifying the cloud types from the satellite images. However, since 22 percent of the cases have moist layers exceeding 10,000 feet in thickness, it may be partly the result of cloud-thickness over-estimation when using a dewpoint depression $\leq 5°C.$ as the criterion for cloud layers. The majority of the C(M) distributions has large moisture thicknesses. The few small thicknesses could be associated with thin layers of middle cloud. The vast majority of the clear observations occur in range 1, as may be expected.

3.1.8 Vertical Temperature Differences

The distributions of vertical temperature differences are shown in Figures 23 to 25, and their means, modes and medians are listed in Table IV. The labelling is the same as that used for the dewpoint depressions. Few differences in the distributions are apparent for a given pair of levels. This means that little significant difference is observed in the stability between pairs of levels for the various cloud and clear categories.

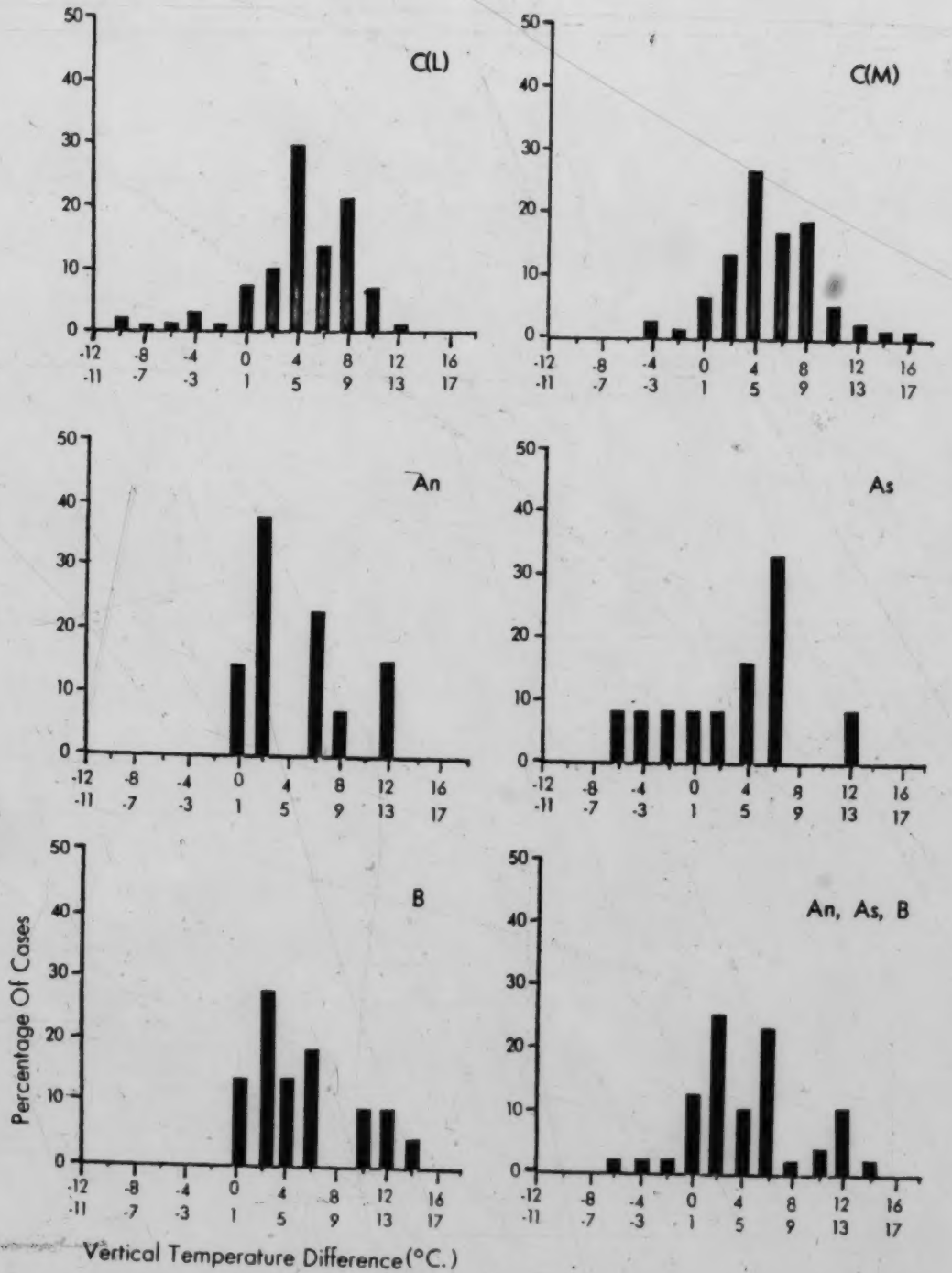

Fig. 23. Temperature (surface) - Temperature (850 mb.) distributions.

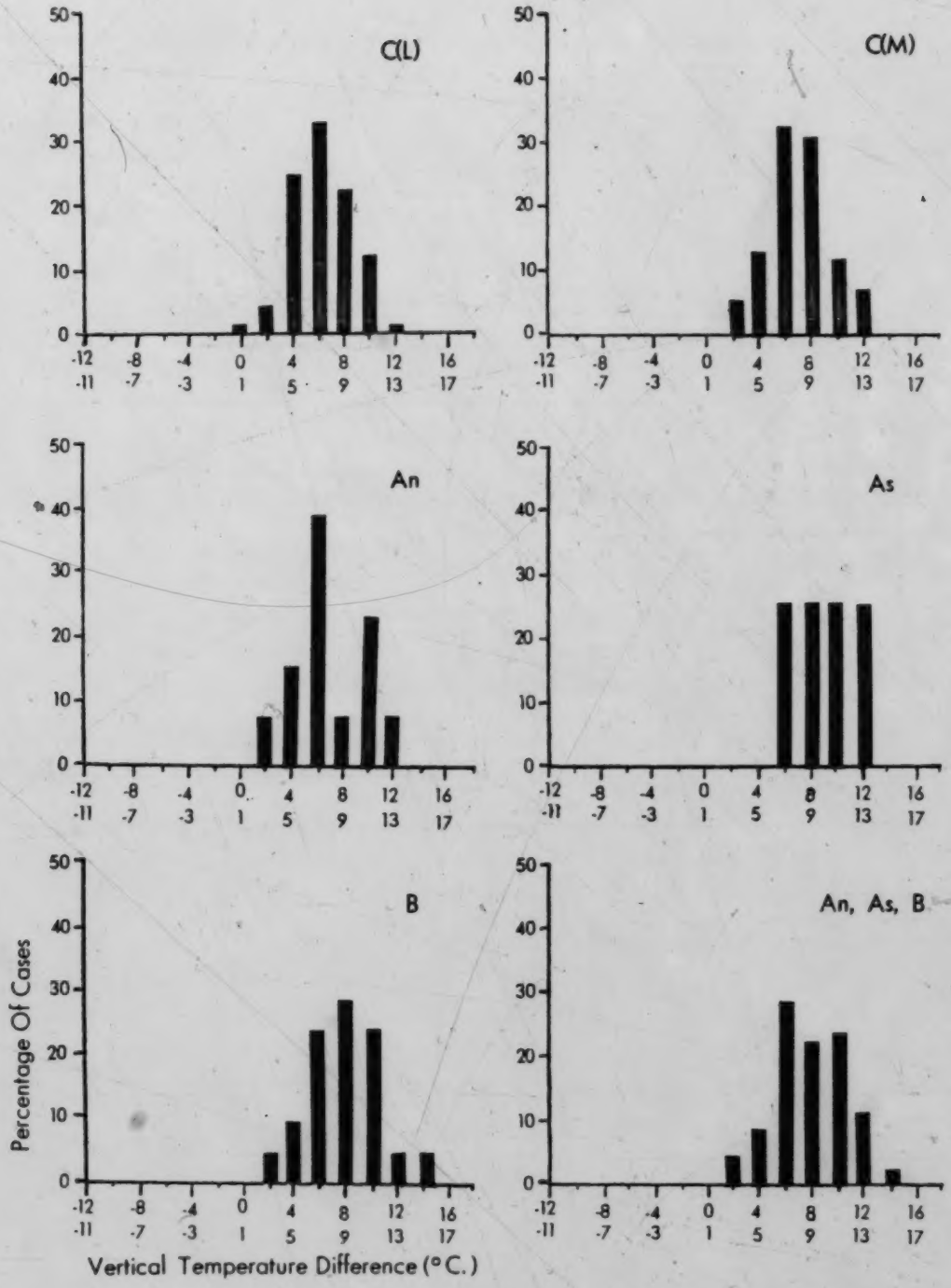

Fig. 24. Temperature (850 mb.) - Temperature (700 mb.) distributions.

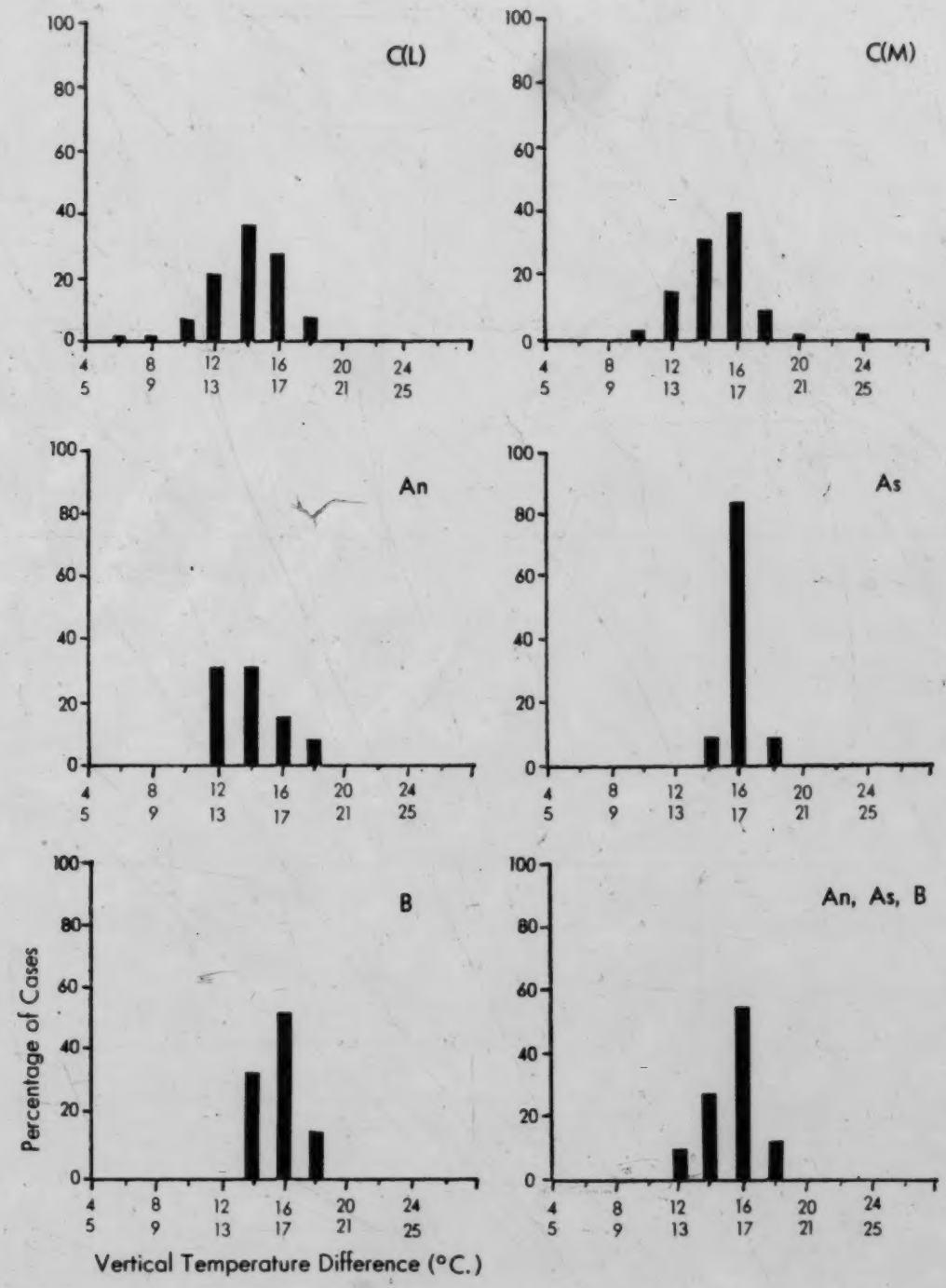

Fig. 25. Temperature (700 mb.) - Temperature (500 mb.) distributions.

Table IV

Vertical temperature difference statistics
for low, middle cloud and clear areas

Class	Mean	Mode	Median	No. of observations
Temperature (Surface)-Temperature (850 mb.)				
C(L)	4.8	4.5	~4.6	98
C(M)	5.6	5.0	~4.9	73
An, As, B	4.8	3.0	~3.7	46
Temperature (850 mb.)-Temperature (700 mb.)				
C(L)	6.7	7.0	~6.3	98
C(M)	7.5	8.0	~7.0	71
An, As, B	8.4	7.0	~7.7	46
Temperature (700 mb.)-Temperature (500 mb.)				
C(L)	15.4	14.0	~14.1	98
C(M)	15.4	16.0	~15.0	72
An, As, B	15.8	16.0	~16.4	46

3.1.9 The "Log-Normal" Transformation

The "log-normal" transformation may be applied to a distribution which is positively skew ($\gamma_1 > 0$) and leptokurtic ($\gamma_2 > 0$) in an effort to obtain a new, more closely normal, distribution.

One transformation will be done to illustrate the procedure. The example to be transformed is the surface dewpoint depression distribution for the C(L) area shown in Figure 17. The details of the calculations for the transformation are given in Appendix A. The resulting transformed distribution is shown in Figure 26. This new distribution appears closer to normal and could be compared statistically with other, similarly transformed, distributions.

3.2 The Vertical Velocity Calculations

3.2.1 Vertical-Velocity Program Test

To compare vertical velocities calculated using the vorticity and omega equation methods, both programs were run on an identical 12 x 12 grid of geopotential heights as a test field. Referring to Figure 3, with the top edge of the grid labelled I = 1, the heights increase uniformly with increasing index I. On the schematic cross-section, Figure 27, the geopotential height gradient increases with height from 20 geopotential

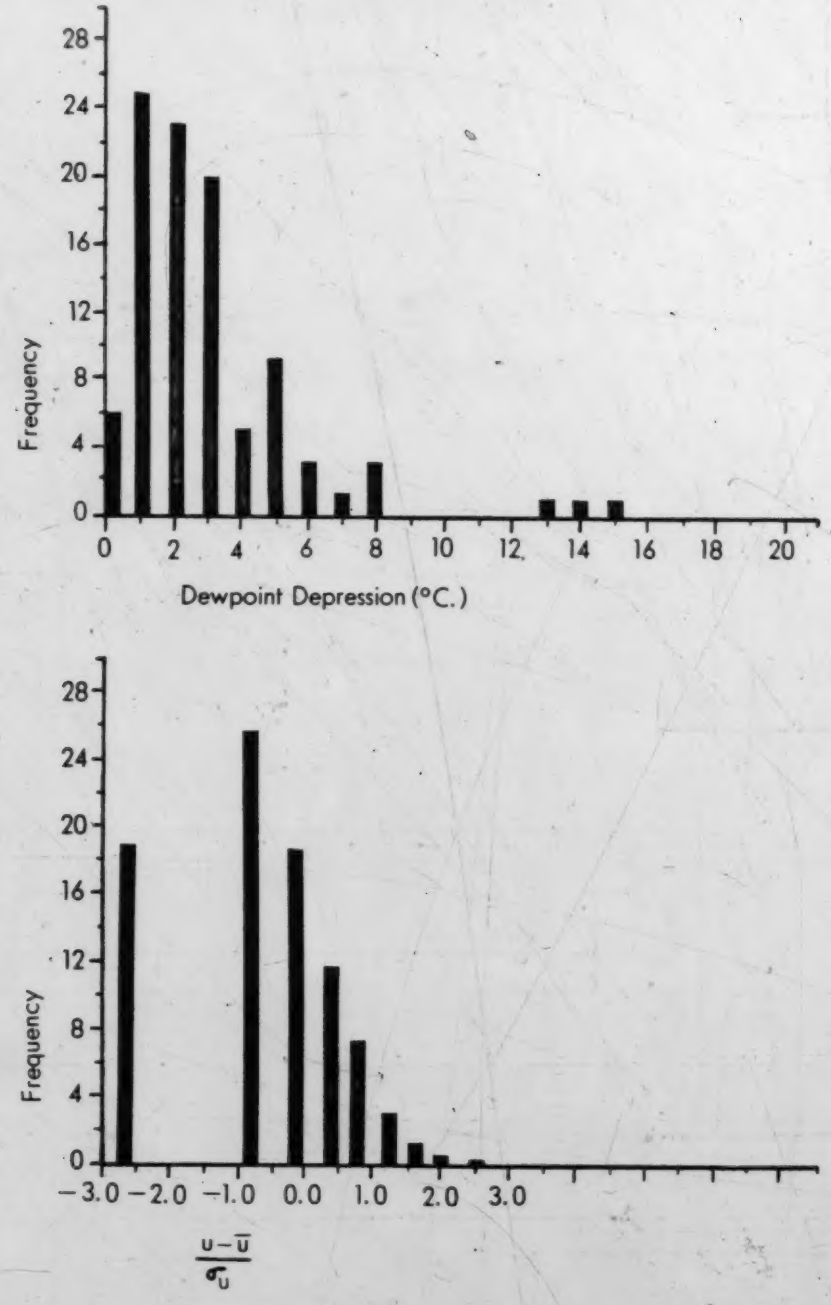

Fig. 26. Dewpoint depression frequencies (upper) and transformed variable frequencies (lower).

metres (gpm) per grid length at 850 mb. to 50 gpm per grid length at 300 mb. Thus, the geostrophic wind speed and direction at a given level are the same, but the speed increases with height. The gridpoint vorticity differences are due only to variations in latitude. Under these conditions the vertical velocities result solely from the advection by the geostrophic wind of the Coriolis component of absolute vorticity.

In Figures 28 to 31, the results of the computations using this test field are shown. For the vorticity method, the calculated vertical velocities increase steadily from low values at 850 mb. to high values at 300 mb.; a consequence of the increasing geopotential height gradient with height. However, the omega equation results show a slight increase in vertical velocities between 775 mb. and 600 mb., followed by a decrease at 400 mb. A possible cause of this discrepancy is that the vertical velocity at the 200-mb. upper boundary is set to zero for the omega equation calculations. This results in a large second derivative of ω with respect to p, a situation which is remedied in the solution of the omega equation by reducing the ω-value at 400 mb.

At the lowest computation levels, the vertical velocities obtained from the two methods are, however, in excellent agreement. For example, at I = 6, J = 6, the 775-mb. omega equation velocity is 0.031 μb. sec.$^{-1}$,

the same value as the average of the 700- and 850-mb. vorticity method vertical velocities. For this study, the 775- and 600-mb. ω - values are used so that errors in ω at 400 mb. should not seriously affect the results.

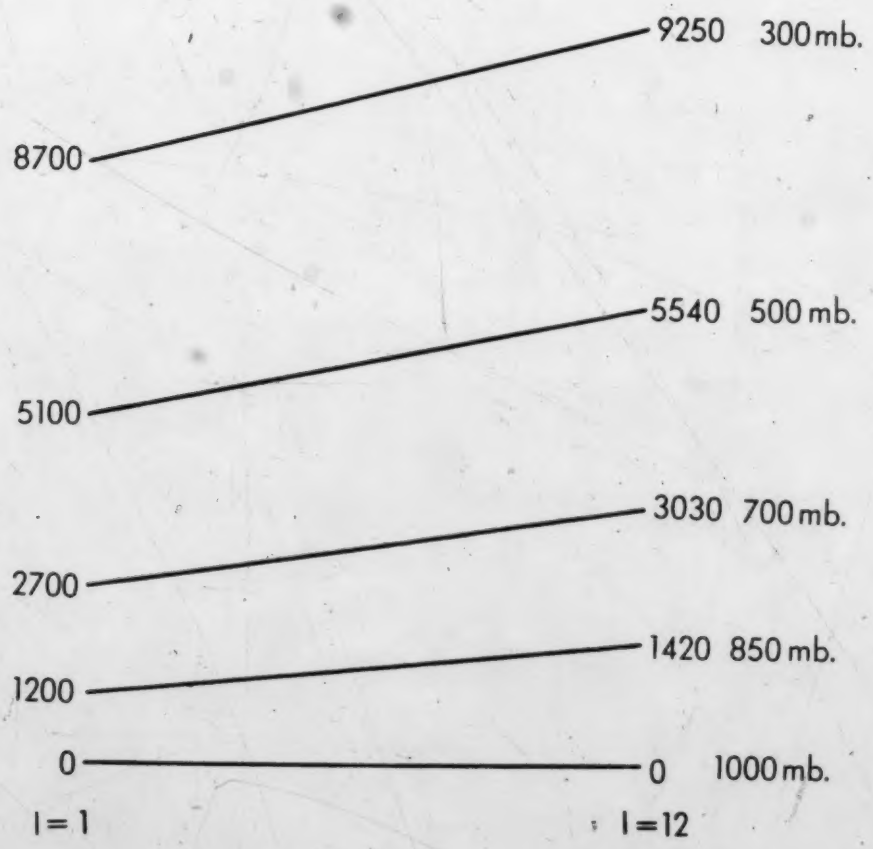

Fig. 27. Vertical cross-section of model atmosphere, showing isobaric surfaces and geopotential heights used in testing vorticity and omega equation methods of vertical velocity calculations.

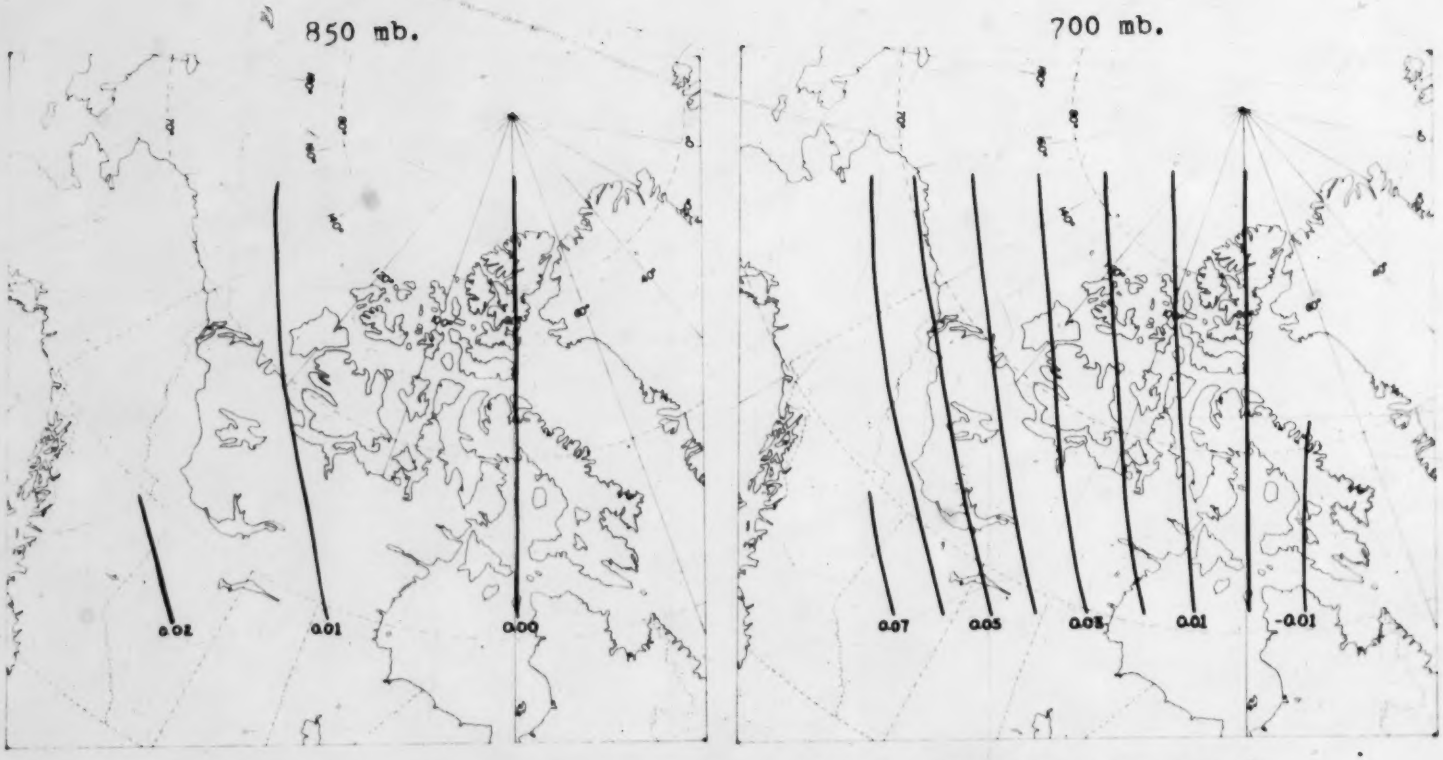

Fig. 28. 850-mb. and 700-mb. vertical velocities (μb.sec.$^{-1}$) generated by the vorticity method for the geopotential test field.

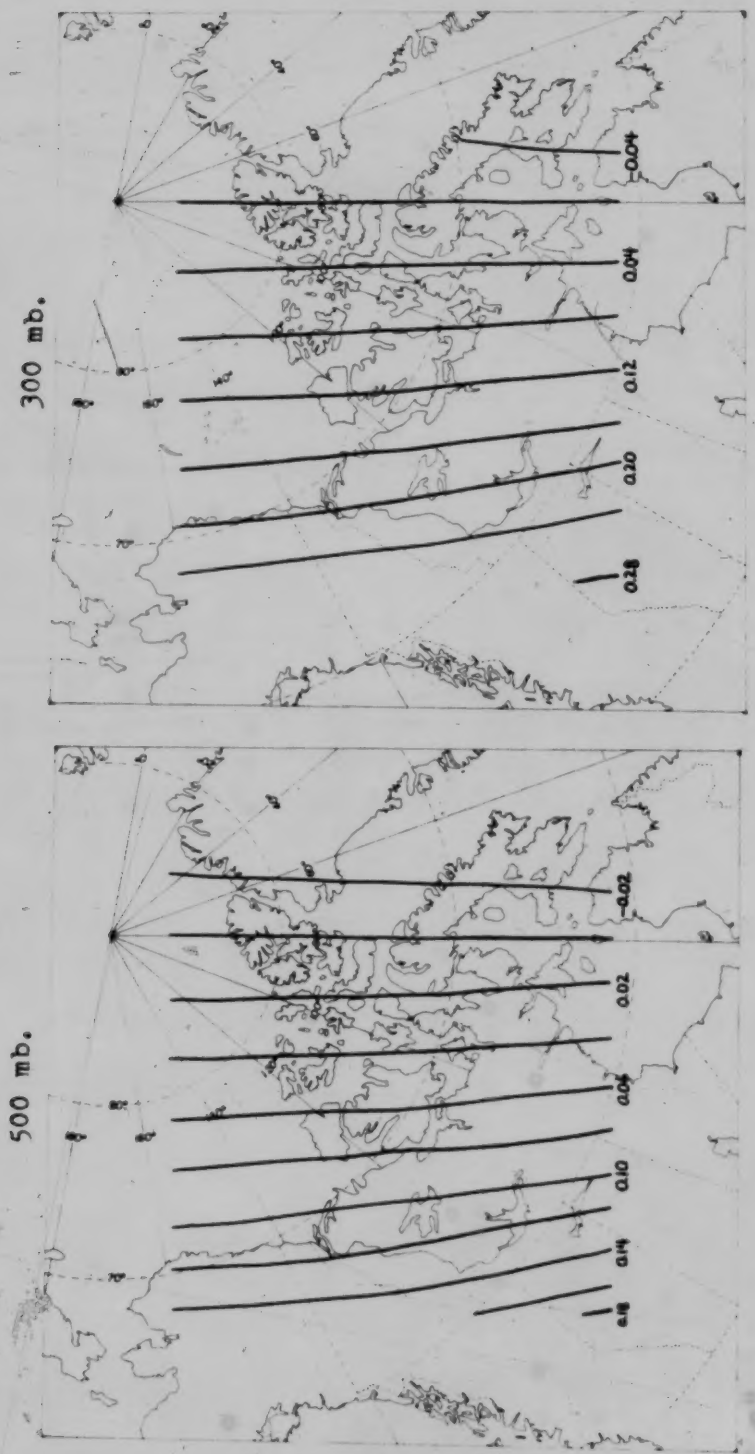

Fig. 29. Same as Fig. 28 except for 500 mb. and 300 mb.

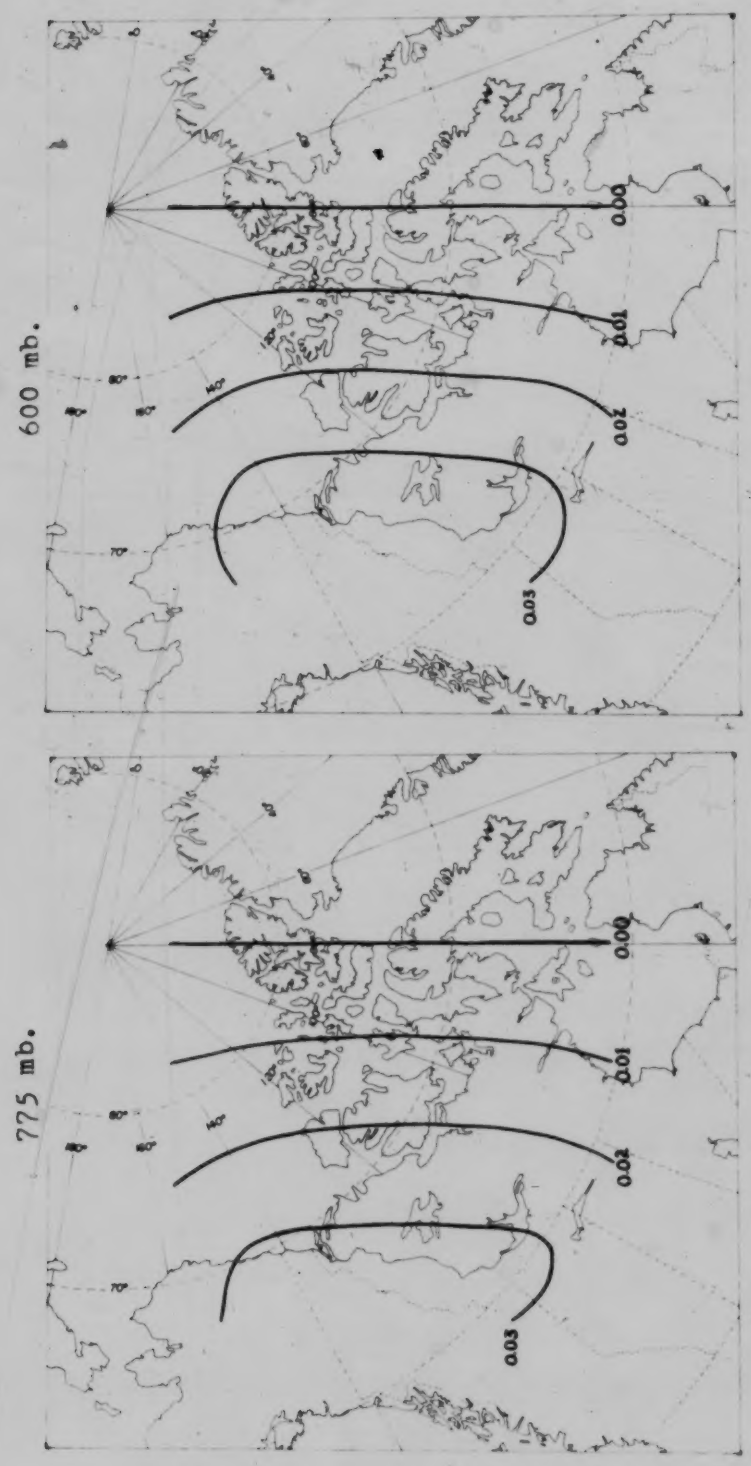

Fig. 30. 775-mb. and 600-mb. vertical velocities ($\mu b.sec.^{-1}$) generated by the omega equation for the geopotential test field.

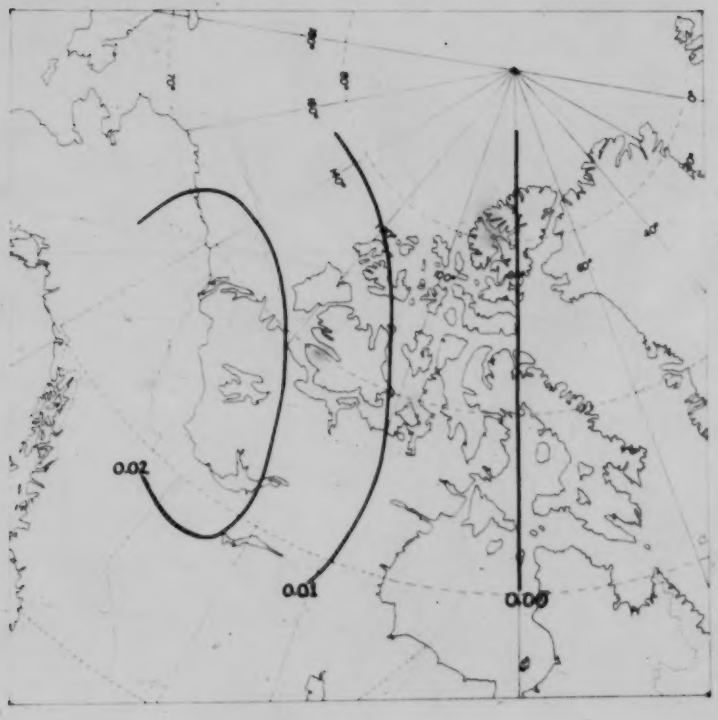

Fig. 31. Same as Fig. 30 except for 400 mb.

3.2.2 Vertical Velocity, Moisture and Cloud

Vertical velocities were calculated for 19/0000 Z to 31/1200 Z, July, 1973 at the inner 8 x 8 gridpoints of Figure 3. Cloud observations, classed as low, middle of clear, were then taken at these gridpoints from the satellite images. Also noted was the moist layer thickness observed by the radiosonde station nearest to a given gridpoint, and in the same cloud or clear area.

The results for the vorticity method of ω - calculations are shown in Tables V-VIII. For Table V, the labels low, middle, clear 1, and clear 2 are, respectively, low cloud using 850-mb. ω -values, middle cloud using 700-mb. ω -values, and clear using 850-mb. and 700-mb. ω -values. The body of the table contains the percentages of observations for each vertical velocity-moist layer combination with the total number of observations shown in brackets.

Omega equation vertical velocities, calculated at 775 mb. and 600 mb., are shown in Tables VIII and IX.

Table V

Percentage occurrences of combinations of vertical velocity (by vorticity method) and moist layer thickness ranges

Moist Layer Thickness (feet)		Vertical Velocity (μb.sec.$^{-1}$)					
		V ≤ -1.0	-1.0<V≤-0.5	-0.5<V≤0.0	0.0<V≤0.5	0.5<V≤1.0	V>1.0
0≤M<2000	Low (81)	0.0	0.0	2.5	1.2	0.0	0.0
	Middle (71)	1.4	1.4	1.4	2.8	1.4	0.0
	Clear 1 (83)	0.0	7.2	42.1	37.3	2.4	0.0
	Clear 2 (83)	4.8	18.0	30.1	20.4	10.8	4.8
2000≤M<8000	Low	0.0	6.2	19.8	35.8	6.2	0.0
	Middle	2.8	7.0	7.0	4.2	0.0	1.4
	Clear 1	0.0	0.0	7.2	3.6	0.0	0.0
	Clear 2	0.0	0.0	7.2	2.4	1.2	0.0
M≥8000	Low	0.0	1.2	14.8	9.9	2.5	0.0
	Middle	8.5	8.5	15.4	16.9	9.9	9.9
	Clear 1	0.0	0.0	0.0	0.0	0.0	0.0
	Clear 2	0.0	0.0	0.0	0.0	0.0	0.0

Table VI

Percentage occurrences of
moist layer thickness ranges

Moist Layer Thickness (feet)	Low (81)	Middle (71)	Clear (83)
$0 \leq M < 2000$	3.7	8.5	89.1
$2000 \leq M < 8000$	67.9	22.5	10.8
$M \geq 8000$	28.4	69.0	0.0

Table VII

Percentage occurrences of vertical velocity ranges using vorticity method

Vertical Velocity (ub.sec.)	Low (115)	Middle (92)	Clear 1 (97)	Clear 2 (97)
$V \leq -1.0$	0.0	12.0	1.0	7.2
$-1.0 < V \leq -0.5$	9.6	15.2	7.2	16.4
$-0.5 < V \leq 0.0$	37.4	26.1	48.4	36.0
$0.0 < V \leq 0.5$	46.1	26.1	39.1	20.6
$0.5 < V \leq 1.0$	7.0	10.9	2.0	12.3
$V > 1.0$	0.0	9.8	2.0	7.2

Table VIII

Same as Table V except using the omega equation vertical velocity results

Moist Layer Thickness (feet)		Vertical Velocity ($\mu b.sec.^{-1}$)					
		$V \leq -1.0$	$-1.0 < V \leq -0.5$	$-0.5 < V \leq 0.0$	$0.0 < V \leq 0.5$	$0.5 < V \leq 1.0$	$V > 1.0$
$0 \leq M < 2000$	Low (81)	0.0	0.0	3.7	0.0	0.0	0.0
	Middle (71)	0.0	0.0	5.6	1.4	1.4	0.0
	Clear 1 (83)	0.0	0.0	41.0	41.0	6.0	1.2
	Clear 2 (83)	0.0	1.2	37.3	41.0	6.0	3.6
$2000 \leq M < 8000$	Low	2.5	0.0	19.8	34.6	7.4	3.7
	Middle	2.8	9.9	8.5	0.0	1.4	0.0
	Clear 1	0.0	0.0	3.6	7.2	0.0	0.0
	Clear 2	0.0	0.0	2.4	8.4	0.0	0.0
$M \geq 8000$	Low	0.0	2.5	11.1	12.3	2.5	0.0
	Middle	2.8	8.5	29.6	19.7	8.5	0.0
	Clear 1	0.0	0.0	0.0	0.0	0.0	0.0
	Clear 2	0.0	0.0	0.0	0.0	0.0	0.0

Table IX

Same as Table VII except
using omega equation vertical velocity results

Vertical Velocity (ub.sec.)	Low (115)	Middle (92)	Clear 1 (97)	Clear 2 (97)
V≤-1.0	1.7	5.4	0.0	0.0
-1.0<V≤-0.5	5.2	16.3	1.0	2.1
-0.5<V≤ 0.0	35.7	45.7	44.3	41.2
0.0<V≤ 0.5	41.7	22.8	45.4	45.4
0.5<V≤ 1.0	13.0	9.8	7.2	7.2
V> 1.0	2.6	0.0	2.1	4.1

For the vorticity method, correlations of cloud with moisture and ascent, or of clear areas with descent and no moisture appear poor. For example, for the low cloud category in Table V , in the 2000 to 8000 feet range, there were more observations of weak subsidence (35.8 percent) than weak ascent (19.8 percent). For the clear 2 cases, in the 0 to 2000 feet range, 30.1 percent of the cases show weak ascent, and only 20.4 percent show weak descent. These poor correlations are also confirmed in Table VII. However, in Table VI, it may be seen that the cloud observations are discriminated much better by moisture alone. That is, the largest percentages of clear, low and middle cloud cases have moisture thicknesses 0-2000 feet, 2000-8000 feet and greater than 8000 feet respectively.

From the omega equation results, the ascent-cloud and descent-clear correlations are improved. In Table VIII, both clear categories for moisture thickness 0 to 2000 feet show more subsidence than ascent. For middle cloud with $M \geq 8000$ feet, more cases of ascent are observed. However, for the low cloud cases for $2000 \leq M < 8000$ feet, more subsidence occurs. Table IX also shows this improvement, as the clear areas show more subsidence and the middle cloud areas more ascent. Again, the low cloud category has few cases of ascent.

Possible reasons for this slight improvement may be the following: since a centred time-derivative of absolute vorticity Q must be calculated in the vorticity method with Q calculated every twelve hours, an error may result in ω due to 24-hour time-derivative smoothing. Also, the thickness term, present in the omega equation, allows for thermal advection while in the vorticity method, no thermal advection can occur. In the case study in Chapter IV, the affect of this term is shown.

For both vertical velocity methods, the low cloud results are the worst. This may be expected since 775 mb. and 850 mb., the levels used for the cloud-vertical velocity calculations, are often above the low cloud and thus are not representative levels for the cloud.

CHAPTER IV

CASE STUDY 23/1200 Z, JULY,1973

4.1 Introduction

The purpose of this case study is to examine cloud patterns on satellite infrared images and correlate them with synoptic features such as lows, troughs and TROWALS, as well as with the distribution of moisture, vorticity and vertical velocity.

This case was chosen because the cloud vortex, associated with a 500-mb. low centre, was located over the Arctic Islands where conventional data coverage was adequate for comparative analysis with satellite infrared images of sufficient quality and resolution. The case study is part of the 19/0000 Z to 31/1200 Z, July, 1973 period, for which geopotential height data and vertical velocities were available.

4.2 Surface Analysis

The surface analysis, Figure 32(b), and the satellite images, Figures 33, 34 show a cloud vortex southwest of Thule (THU), close to the surface low over southern Ellesmere Island. The TROWAL over northwestern Greenland (see Figure 32(b)) shows up as a band of cloud on the satellite images, and as tongues of warm

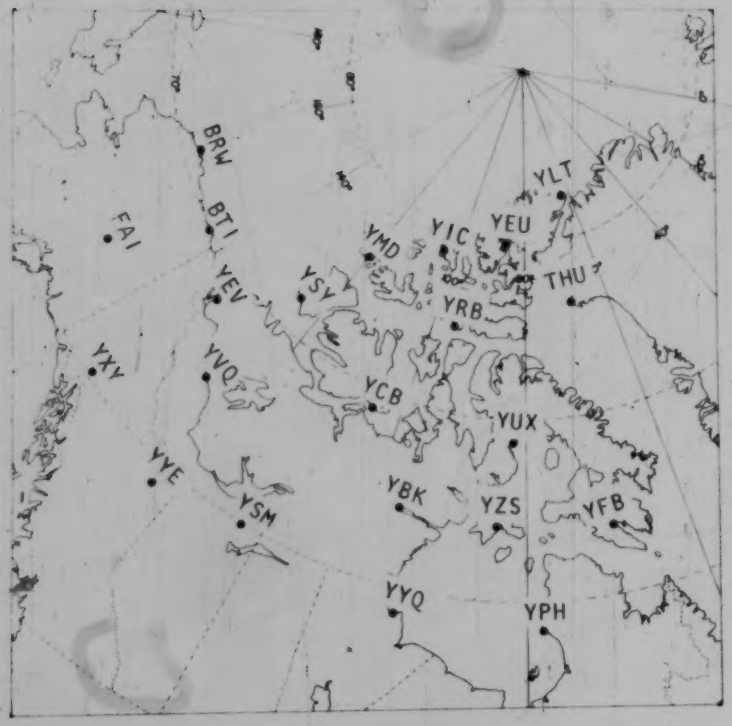

Fig. 32(a)

Locations of radiosonde stations. Three-letter code denotes station identifiers.

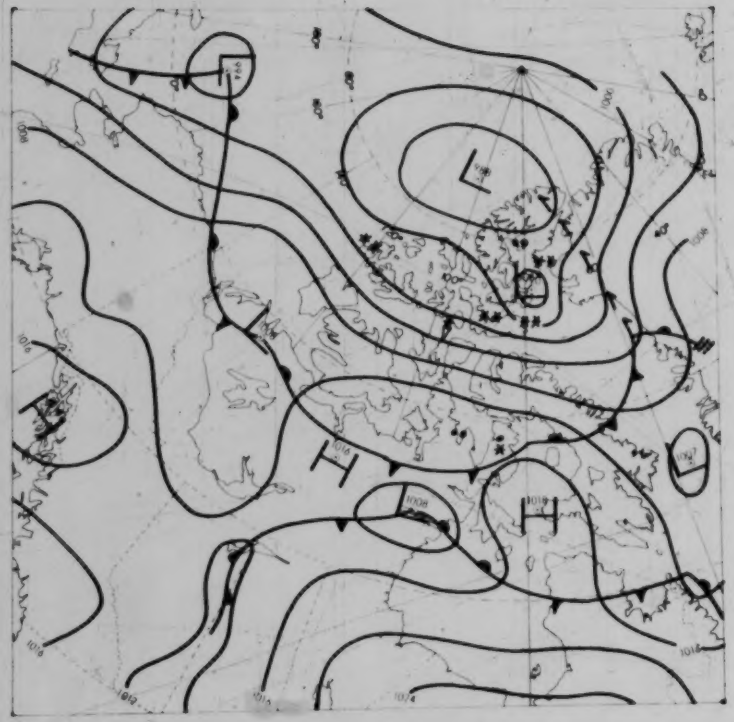

Fig. 32(b)

Surface analysis for 23/1200 Z, July, 1973.

39

Fig. 34. NOAA-2, 3521.
23/2200Z, July, 1973.

air on the 850- and 700-mb. charts, Figures 35(b) and 36(b). The bright white cloud over the Foxe Basin is associated with a surface wave east of Hall Beach (YUX) and a 1008-mb. low centred near Baker Lake (YBK). The cold front extending from the 1008-mb. low southwestward is well marked on the satellite image by a line of clouds. A band of cloud appears also to the north of the surface warm front, over the Beaufort Sea.

4.3 850-mb. Analysis

On the 850-mb. chart, Figure 35(a), areas of low cloud are outlined by wavy lines and labelled C(L). Moist areas with dewpoint depressions DD $\leq 5^{\circ}$C are labelled M. The moist areas near Mould Bay (YMD), northeast from Resolute Bay (YRB) and along the Alaskan coast coincide well with the areas of low cloud. The low cloud from Hall Beach to north of Great Slave Lake and northwestward occurs in what appears to be a dry area. However, since this is an area with very few weather observing stations, correspondence between the cloud and moisture patterns is likely to be unsatisfactory.

4.4 700-mb. Analysis

At 700 mb., Figure 36(a), the C(M) areas denote middle cloud. The cloud and moisture regions coincide

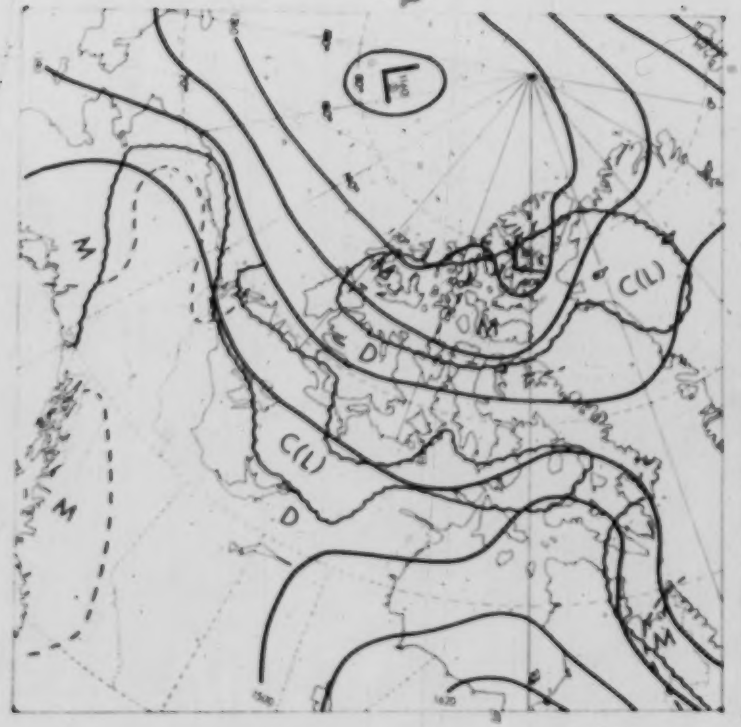

Fig. 35(a)

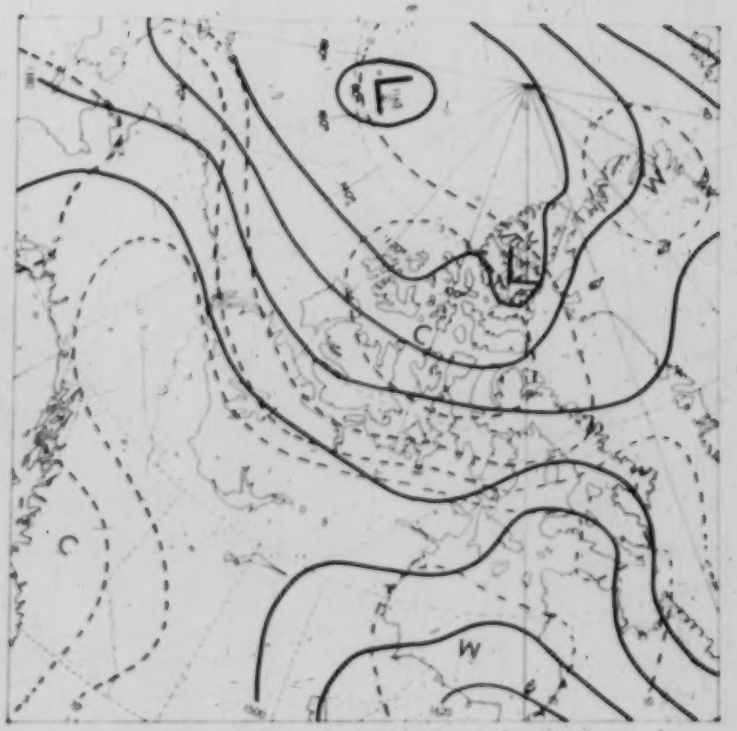

Fig. 35(b)

850-mb. contour chart for 23/1200 Z, July, 1973, including low cloud C(L) and moisture analyses. M denotes regions with dewpoint depressions DD≤ 5°C.

850-mb. contour chart for 23/1200 Z, July, 1973, with isotherms drawn at 5°C. intervals.

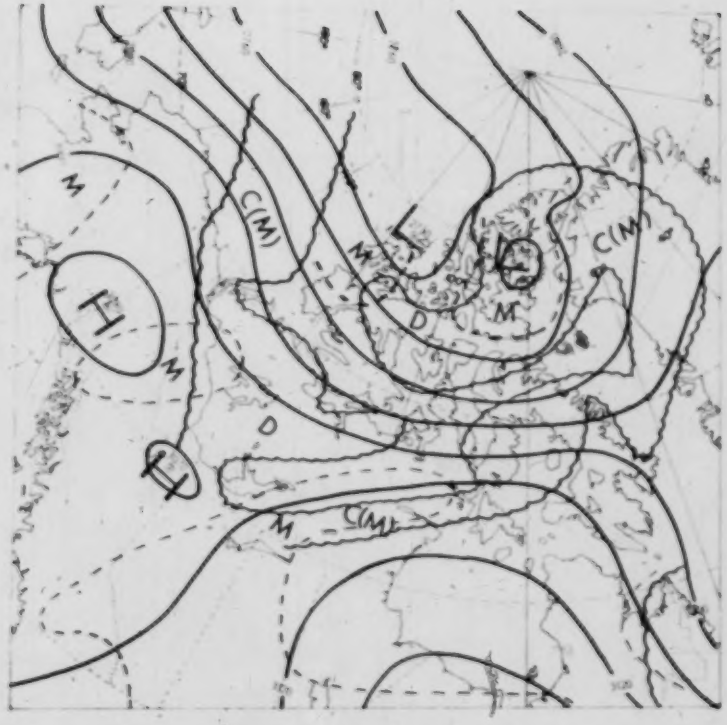

Fig. 36(a)

700-mb. contour chart for 23/1200 Z, July, 1973, including middle cloud C(M) and moisture analyses. M denotes regions with dewpoint depressions DD≤ 5°C.

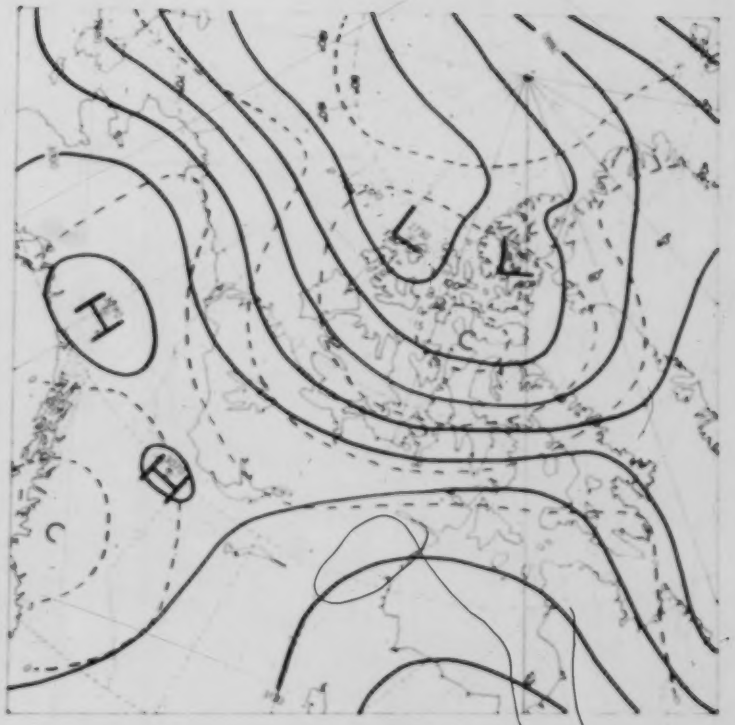

Fig. 36(b)

700-mb. contour chart for 23/1200 Z, July, 1973, with isotherms drawn at 5°C. intervals.

quite well over Ellesmere Island, from Baker Lake southwestward, and in the Norman Wells (YVQ) area. However, northeast of Norman Wells and over the Beaufort-Sea, middle cloud appears on the satellite image but no moisture correlations can be made without radiosonde stations in these areas.

4.5 500-mb. Analysis

A strong short-wave trough, from the vorticity centre 22 x 10^{-5} $sec.^{-1}$ southward to Hall Beach, has positive vorticity advection and a cloud shield to the east of it. A second trough, from west of Cambridge Bay (YCB) to Great Slave Lake has a weak positive vorticity advection area and narrow bands of cloud east of it. Upstream from this trough, there is negative vorticity advection and middle cloud. This will be considered further in Section 4.7.

4.6 Vertical Velocity-Low Level

Since low cloud frequently is below the 775-mb. and 850-mb. levels, the vertical velocity and low cloud patterns may not correlate well. This is evident in Figures 38(a) and 39(a). The low cloud-ascent areas coincide over Northern Greenland, Ellesmere Island and from Hall Beach to north of Baker Lake but not in the areas west of Baker Lake to Great Bear Lake and Inuvik.

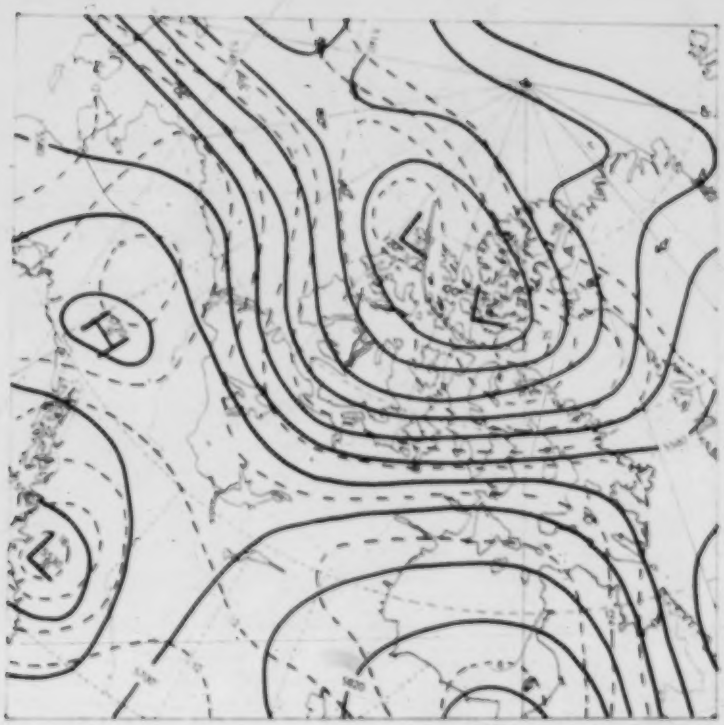

Fig. 37. 500-mb. contour and vorticity chart for 23/1200 Z, July, 1973.

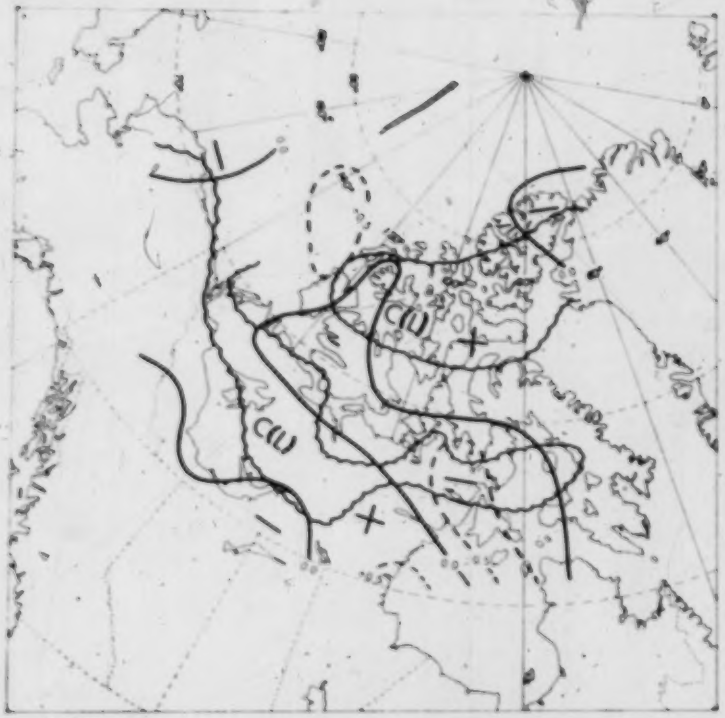

Fig. 38(a)

Vertical velocity field by vorticity method at 850 mb. and low cloud for 23/1200 Z, July, 1973.

Fig. 38(b)

Vertical velocity field by vorticity method at 700 mb. and middle cloud for 23/1200 Z, July, 1973.

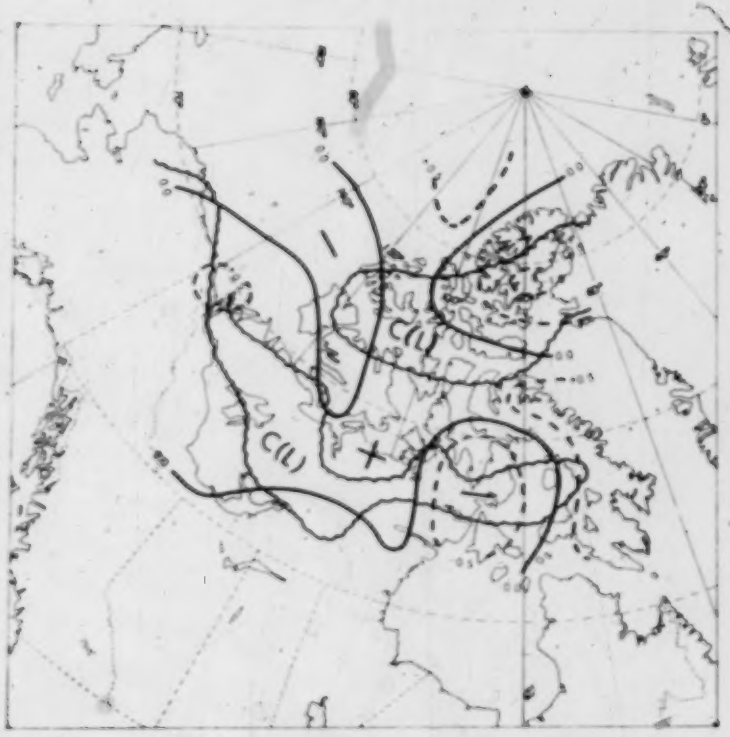

Fig. 39(a)

Vertical velocity field by omega equation method at 775 mb. and low cloud for 23/1200 Z, July, 1973.

Fig. 39(b)

Vertical velocity field by omega equation method at 600 mb. and middle cloud for 23/1200 Z, July, 1973.

In the central Arctic Islands the omega equation vertical velocities show better ascent-cloud correlations.

4.7 Vertical Velocity - Middle Level

Figures 38(b) and 39(b) show the 700-mb. and 600-mb. vertical velocity patterns. At each level, middle cloud and ascent occur in the Ellesmere Island-northern Greenland areas but the omega equation results indicate closer vertical velocity-cloud correlations. Ascent and middle cloud also occur together from Hall Beach to the vicinity of Fort Smith (YSM). However, both vertical velocity calculations generate subsidence in the vicinity of 75°N between 80°W and 100°W and from Great Slave Lake to Inuvik. The major difference between the vertical velocity calculations appears north of the Alaskan coast. At 500 mb., since negative vorticity advection is occurring, subsidence is expected and is evident in Figure 38(b). However, the omega equation generates ascent in this same area. Since the thermal pattern at 700 mb. (see Figure 36(b)) indicates warm air advection and a thickness advection term is included in the omega equation, it is this warm air advection which is causing the ascent. Thus, the omega equation is superior in this instance because it includes both thickness advection and vorticity.

CHAPTER V

PROBLEMS ENCOUNTERED AND SUGGESTIONS FOR IMPROVEMENTS

5.1 Cloud Classification

As noted earlier in Chapter I, the cloud classification derived from satellite infrared images is based on a "grey-scale" of varying shades corresponding to the radiating temperatures of the cloud masses scanned. Occasionally problems may arise with broken middle cloud, if the cloud and clear patches are below the resolution of the infrared scanner. According to Anderson et al (1973), if there are several sources of radiation below the resolution of the sensor, the receiver integrates the radiances into a single response. Thus, for broken middle cloud, the scanner will respond to an average temperature, and produce an intermediate shade of grey composed of the dark grey of the warm Earth's surface, and the white of the cold cloud mass. The resulting shade of grey may lead to an incorrect classification of middle cloud as low cloud. Similar problems have been encountered by Glahn (1966). He found that individual cloud elements with a diameter slightly less than the resolution area of the infrared scanner can have their tops judged to be several thousand feet below their actual height.

A problem also arises in the classification of clouds as only middle or low, depending on their grey shade. A more precise determination of the cloud top heights would be an improvement as then the meteorological parameters associated with the cloud could be found more accurately. A possible way to find the cloud top heights would be to use a grey scale for comparison with satellite image grey shades. For an image, the grey shade of a surface at a known temperature (e.g. an open water area under clear skies) could be compared to the grey scale. The temperatures corresponding to other shades of grey on the scale could be found relative to this known "reference" grey shade temperature. Then, the shades of other areas on the satellite image could be compared to the grey scale to determine the temperatures of the radiating areas. From radiosonde reports, the cloud top heights could then be found along with the corresponding meteorological parameters.

5.2 Vertical Velocity - Cloud Correlations

As was evident in the vertical velocity contingency tables given in Chapter III, the expected correlations between ascent and low cloud were often poor. One reason for this is that the vertical velocity is calculated at a level above the low cloud layer. To

improve the correlations, vertical velocities produced by surface terrain and friction in the boundary layer should be calculated and correlated with the low cloud.

Barr et al. (1966) studied patterns of vertical velocity associated with cloud vortices over the northeastern United States. They found that both horizontal and vertical motions are important in large-scale cloud systems. The vertical velocities, calculated using the omega equation, show reasonable agreement with cloud patterns. However, the authors noted that since the cloud element sizes on the satellite images can be several orders of magnitude smaller than the scale at which the vertical velocities are calculated (in their study, the grid-length was 165 km.), only the broader aspects of the cloud patterns may be expected to correlate well with the vertical motions. In this study, with a grid-length of 381 km., the point-by-point comparisons of vertical velocities and cloud showed generally poor results. However, in the case study, the broad aspects of the cloud and vertical velocity patterns coincided fairly well.

Barr et al (1966) also stressed the importance of horizontal motions in the maintenance of cloud systems. In their analysis, a simple trajectory model was used in which air parcels are advected by the wind along a surface

of constant pressure. In this way, a rough estimate of the history of the vertical motion of the parcel may be made before the time of the cloud analysis. This was done by observing the vertical motion areas for several hours before the time of the cloud observations. They found that, frequently, a mass of cloud, observed within an area of descent at the time of the vertical velocity calculation, may have been in an area of ascent for several hours prior to the observation time. In such cases, the net vertical velocity can be ascent, while the descent, which may be occurring at the time of the cloud observation is too short or too weak to dissipate the cloud.

Barr et al (1966) also found that the vertical motion correlated best with the cloud patterns early in the vortex development stage, before an extensive cyclonic circulation developed. Once a closed circulation has been set up, dry, clear air rotates around the eastern areas of the vortex into the ascent area, and moist, cloud-bearing air circulates around the northern parts into the area of descent west of the vortex centre. The 500-mb. lows examined in the present study had closed and well-developed circulations which usually persisted for several days. Since quasi-rotary motion of cloudy and clear areas within a vortex is a common feature of the atmospheric

circulation, the use of even a fairly crude trajectory model may improve the correlations between the vertical motion and the cloud patterns.

A final point concerns the nature of the vertical motion calculation. The superiority of the omega equation method has already been demonstrated by its ability to include thickness advection. However, neither the omega nor the vorticity method include diabatic terms in the vertical velocity determinations. Bullock et al (1969) compared vertical motions resulting from diabatic and adiabatic processes separately. The diabatic process considered was terrestrial radiation. They found that, for clear skies, the infrared radiation contributes considerable downward motion to the airmass. Since vertical velocities, determined in the present study, are quite small, this positive vertical velocity due to the infrared components, if included, could have a significant effect on the adiabatic vertical velocities. It could reverse the vertical velocity sign from negative to positive or it could increase an already positive vertical velocity. For cloudy skies, the mean infrared component of the vertical velocity in the Bullock et al (1969) study shows negative vertical velocities just below the cloud base, and positive values just above the cloud layer.

Thus, this infrared component could have an influence on the net vertical velocity, depending on the level at which it is calculated relative to cloud layers.

CHAPTER VI

SUMMARY AND CONCLUSIONS

There are several problems in Arctic meteorology for which satellites offer assistance. The sparseness of data is perhaps the foremost difficulty. This is particularly evident over the Beaufort Sea and the vast Arctic Ocean, sources of many low pressure areas that track across the Queen Elizabeth Islands. Satellite coverage, coupled with the recognition of cloud patterns and associated meteorological features, provide for a considerable improvement in the analysis and forecasting for these areas. Satellite image analysis is also valuable in assessing the extent of cloud masses in more data-rich areas. Fog and stratus which may be reported at several high Arctic stations, could be coastal, widespread or topped by much thicker cloud. Satellite information helps to differentiate among the three cases. In the Arctic winter special problems arise where satellite photos are useful. Very low temperatures make radiosonde soundings of moisture unreliable for the determination of saturated atmospheric layers. Again infrared satellite images are helpful in overcoming this problem by the delineation of wintertime cloud masses.

The present study has considered four aspects of Arctic meteorology:

(1) cyclone tracks at 500-mb.,

(2) moisture and temperature distributions in cloud masses associated with upper-level cyclones,

(3) vertical velocities and moisture thicknesses in cloud areas around vortices, and,

(4) the correlation of synoptic features and cloud areas from a detailed case study.

Figures 11 to 16 demonstrate the persistence and complexity of the 500-mb. cyclone paths. Occasionally, a track in a sparse data area appears complex, but the apparent complexity may be the result of the 500-mb. objective analysis scheme. Several more years of data would be required to determine seasonal mean 500-mb. low positions or favoured tracks for these systems.

To determine the moisture and temperature distributions associated with the cloud masses spiralling around these cyclones, a crude cloud-band model was used where clear and cloud areas around a vortex centre were categorized. Subsequently, radiosonde reports from upper air stations located in the various areas in the cloud band model were used to obtain moisture and temperature distributions, as well as central tendencies and dispersion statistics for these areas. The dewpoint depression distributions

were as expected, that is low cloud areas showed positively skew distributions at the surface and 850-mb. and middle cloud areas had positively skew distrubutions at 700-mb. The surface and 850-mb. level, and the 700-mb. level were used as rough approximations for the low and middle cloud levels, respectively. Low 700-mb. dewpoint depressions were occasionally observed in low cloud regions, likely caused by moisture extending above these low cloud areas. Also, moisture sometimes extended below the middle cloud areas, resulting in positively skew surface and 850-mb. dewpoint depression distributions in middle cloud regions.

The uncertainty of the cloud height determined from the satellite images appears to be a major problem encountered in this study. An alternative, using a grey scale to determine the cloud top temperatures and hence their heights, was suggested in Chapter V. For future studies, this should be a considerable improvement over the subjective grey shade determination of low or middle cloud as used here.

To calculate vertical velocities, geopotential height data on a 12 x 12 grid were used, for a two week period in July, 1973. Contingency tables were constructed to determine the percentages of occurrence of combinations of vertical velocities and moist-layer thicknesses. The

results of this work were generally not promising in that regardless of the moisture layer thicknesses, a larger percentage of subsidence was calculated for low cloud areas and more ascent for clear areas, the opposite to that expected. Middle cloud results were better, with a slightly larger percentage of cases showing ascent. Several reasons for these results have been considered. The use of the vertical velocities at 850 and 775 mb., and 700 and 600 mb. as representative of low and middle cloud levels, respectively, is open to question. Again, a more exact estimate of the level of the cloud must be found and used for the vertical velocity level. Computation of terrain-induced vertical velocities, as representative of the vertical motion in low cloud areas, would likely increase the percentage of cases of ascent in low cloud areas, since the latter are frequently surface based.

The methods of computation of the vertical motion have also been questioned. Both calculations include only adiabatic processes of vertical motion, ignoring diabatic processes such as infrared radiation, which, in clear sky conditions, contributes a positive vertical velocity component. In cloud areas the infrared component has a mean negative value just below the cloud base and a mean positive value just above it. Thus, depending on the level of computation of the vertical velocity, the

infrared component could have an effect in cloudy conditions.

Finally, an air parcel trajectory determination has been suggested. Since 500-mb. cyclones have frequently spiralling bands of cloud associated with them, dry, clear air may be intruding into ascent regions, and moist, cloud air into subsidence regions at the time of observations of the satellite image. A trajectory model could be used to determine an approximation of the net vertical motion an air parcel has experienced prior to the satellite image time.

A detailed examination of a case has been done to correlate cloud patterns with synoptic features. In regions with upper-air data, the 700-mb. and 850-mb. moist areas coincided fairly well with the satellite cloud areas. At 500 mb., the positive vorticity advection areas, in most cases, had cloud associated but, in one instance, negative vorticity advection and cloud occurred together. For this same area, positive vertical velocities were calculated by the vorticity method, whereas the omega equation calculations correctly indicated negative vertical velocities. This superiority of the omega equation is partly the result of the thickness advection term. Since warm-air advection was also occurring in the negative vorticity advection area in question, the omega equation correctly predicted ascending motion.

It is hoped that the results of this study will be useful for guidance as a first approximation of the meteorological parameters associated with 500-mb. cyclones. Also, perhaps the problems and pitfalls discussed will be of assistance to others undertaking similar studies using satellite images in the high Arctic.

BIBLIOGRAPHY

Anderson, R.K., Veltishchev, N.F., 1973: The Use of Satellite Pictures in Weather Analysis and Forecasting. World Meteorological Organization Technical Note No. 124, 275 pp.

Barr, S., Lawrence, M.B., Sanders, F., 1966: TIROS Vortices and Large-Scale Vertical Motion. Mon. Wea. Rev., 94, pp. 675-696.

Brooks, C.E.P., Carruthers, N., 1953: Handbook of Statistical Methods in Meteorology. London, Her Majesty's Stationery Office, 412 pp.

Bullock, B.R., Horn, L.H., Johnson, D.R., 1969: The Contribution of Infrared Cooling to the Vertical Motion Field and Its Implication in Atmospheric Energetics. Mon. Wea. Rev., 97, pp. 371-381.

Finney, D.J., 1941: On the distribution of a variate whose logarithm is normally distributed. Supplement, J.R. Statist. Soc., London, 2, No. 7, p. 155.

Glahn, H.R., 1966: On the Usefulness of Satellite Infrared Measurements in the Determination of Cloud Top Heights and Areal Coverage. J. Appl. Meteor., 5, pp. 189[illegible]

Haltiner, G.J., Clarke, L.C., Lawniczak, G.E., 1963: Computation of the Large-Scale Vertical Velocity. J. Appl. Meteor., 2, pp. 242-259.

Haltiner, G.J., 1971: Numerical Weather Prediction. John Wiley and Sons, Inc., N.Y. and Toronto, 317 pp.

Hess, S.L., 1959: Introduction to Theoretical Meteorology. New York, Holt, Rinehart and Winston, 362 pp.

Hume, W.D., 1975: Development of a quasi-geostrophic prediction model for weather systems over Western Canada. M.Sc. Thesis, Univ. of Alberta.

Petterssen, S., 1956: Weather Analysis and Forecasting. Volume I, second edition. McGraw-Hill Book Co., N.Y., 428 pp.

Schram, G.R., 1974: The influence of orography and surface friction on synoptic scale vertical motions over Western Canada. M.Sc. Thesis, Univ. of Alberta.

Shenk, W.E., Brooks, E.M., 1965: Thermal and Wind Structures Related to Major Cloud Bands of TIROS - Photographed Extratropical Vortices. J. Appl. Meteor., 4, pp. 676-692.

Wilson, H.P., 1973: Arctic Operational Meteorology, A Study Guide for Arctic Weather Forecasters. Edmonton, Queen's Printer, 367 pp.

APPENDIX A

A "LOG-NORMAL" TRANSFORMATION

The transformation is for the surface dewpoint depression distribution for the C(L) area shown in Figure 17.

(a) The skewness γ_1 and kurtosis γ_2 are calculated as follows:

For the C(L) surface dewpoint depression distribution, the statistics are given below.

Mean ($\bar{x}$) = 2.9

Variance (μ_2) = 7.2

Standard Deviation (σ_x) = 2.7

Third moment (μ_3) = 58.0

Fourth moment (μ_4) = 710.6

From equation (1.27):

$\gamma_1 = +3.0$

From equation (1.28)

$\gamma_2 = +10.6$

Since both γ_1 and γ_2 are positive, the "log-normal" transformation may be applied.

(b) Using the σ_x given above, ω is calculated from equation (1.31).

$\omega = 0.8$

(c) σ_u is calculated from equation (1.32).

$\sigma_u = 0.7$

(d) Calculate $\frac{u-\bar{u}}{\sigma_u}$ from equation (1.30) for each value of the independent variable x(here the dewpoint depression).

From a table of probability integrals for the normal frequency curve such as Appendix II(c) in Brooks et al (1953), the frequency distribution of $\frac{u-\bar{u}}{\sigma_u}$ was obtained. The original dewpoint depression frequencies and the transformed variable $\frac{u-\bar{u}}{\sigma_u}$ frequencies are shown in Table A-I and plotted in Figure 26.

Table A-I

Dewpoint depression and
transformed variable frequencies

Dewpoint Depression (°C.)	Frequency	Transformed Variable	Frequency of Transformed Variable
0.0	6	-2.6	18.6
1.0	25	-0.9	26.0
2.0	23	-0.1	18.8
3.0	20	0.4	11.9
4.0	5	0.8	7.6
5.0	9	1.0	4.8
6.0	3	1.3	3.0
7.0	1	1.5	2.1
8.0	3	1.7	1.4
9.0	0	1.8	0.9
10.0	0	2.0	0.7
11.0	0	2.1	0.6
12.0	0	2.2	0.4
13.0	1	2.3	0.3
14.0	1	2.4	0.2
15.0	1	2.5	0.2